Doctoral Dissertations   Student Theses and Dissertations

1968

Decomposition of Cr(OH)₃ to form active Cr₂C₃

Timothy A. Clancy

Recommended Citation

DECOMPOSITION OF $Cr(OH)_3$ TO FORM ACTIVE Cr_2O_3

A Dissertation

Presented to

the Faculty of the Graduate School

University of Missouri-Rolla

In Partial Fulfillment

of the Requirements for the Degree

Doctor of Philosophy

by

Timothy A. Clancy

March, 1968

DECOMPOSITION OF $Cr(OH)_3$ TO FORM ACTIVE Cr_2O_3

by

Timothy Allen Clancy, *1940*

A DISSERTATION

Presented to the Faculty of the Graduate School of the

UNIVERSITY OF MISSOURI - ROLLA

In Partial Fulfillment of the Requirements for the Degree

DOCTOR OF PHILOSOPHY

in

CERAMIC ENGINEERING

1968

DECOMPOSITION OF $Cr(OH)_3$ TO FORM ACTIVE Cr_2O_3

An Abstract of a Dissertation

Presented to

the Faculty of the Graduate School

University of Missouri-Rolla

In Partial Fulfillment

of the Requirements for the Degree

Doctor of Philosophy

by

Timothy A. Clancy

March, 1968

ABSTRACT

This study was concerned with the sinterability of Cr_2O_3 powders produced by the calcination of a $Cr(OH)_3$ gel. The decomposition of the gel was investigated by thermogravimetric analysis, X-ray analysis and microscopic examination. Comparison was made between the size of crystallites as determined by X-ray line broadening and the size of aggregated particles as determined by independent means. These lineal measurements were compared to surface area measurements on the calcined powders. The degree of sinterability was judged from the density measurements on Cr_2O_3 pellets fired under air, oxygen and nitrogen atmospheres.

Energies of activation of 25 and 20 kilocalories per mole were found for the decomposition process and the crystallite growth process, respectively. The decomposition process can be described as a unimolecular mechanism obeying first-order reaction kinetics. The calcined powders were found to be composed of small hexagonal platelets arranged in loosely packed aggregates. The optimum calcination temperature was determined to be approximately

500°C. A maximum sintered density of 4.35 grams per cubic centimeter illustrated the effectiveness of a nitrogen sintering atmosphere.

ACKNOWLEDGEMENT

TABLE OF CONTENTS

LIST OF FIGURES

LIST OF TABLES

I. INTRODUCTION

In conventional refractories practice, calcining of
the raw materials is followed by crushing, grinding, and
grading treatments prior to the pressing, drying and firing
processes. The porosities of the conventional products
are normally in the range of 15 to 20 per cent. Many
special applications arose from the growth of refractories
and metals after World War II, making the importance of
the effects of porosity on the properties come to be more
appreciated and, consequently, much attention was paid to
fabrication processes and sintering behavior. In such
studies, it was inevitable that consideration be given to
the preparation of powders by lower temperature processes
(such as thermal decomposition of compounds) since "dead
burning" or the use of high-temperature processes was
known to have deleterious effects on the reactivity of
the powder.

One important feature that has emerged from studies of
the sintering process is that densification proceeds, pri-
marily, by the elimination of inter-connected or open
porosity, the proportion of closed porosity remaining at a
constant low level. The demand for impermeability makes

severe demands on the control of the sintering process
and on the nature of the powders being used. The driving
force in sintering is generally assumed to be the excess
of surface free energy of a powder over that of the same
material in the dense form. This energy should increase
with decrease of particle size for a constant weight of
material. For a given pore volume, the overall permeability
will diminish with a decrease in size of pores. Thus, all
factors argue in favor or the use of the finest particles.
However, there are other factors, such as particle shape
and size distribution, which can play an important role in
sintering behavior. It is also important to be able to
describe the powder from the standpoint of the decomposition
process of the parent compound.

The purpose of this research was to study the formation
of "active" Cr_2O_3 powders by the decomposition of $Cr(OH)_3$
and the sintering behavior of these powders. The properties
of Cr_2O_3, as listed in Table (1), indicate that an excellent
refractory body could be made from this oxide. The specific
approaches to the analysis of Cr_2O_3 was to study the decom-
position of $Cr(OH)_3$ by thermogravimetric analysis, to
characterize the various calcines by X-ray analysis, particle
size and surface area measurements and microscopic exami-
nation and to study the sintering behavior of selected
calcines under several atmospheric conditions.

TABLE 1.

Properties of Cr_2O_3

Density: 5.21 gm/c.c.

Crystal Structure: hexagonal close-packed

Space Group: $R\overline{3}c$ or D_{3D}^6

Solubility: insoluble in acids and alkali;
               slightly soluble in molten $KHSO_4$

Color: green

Index of Refraction: 2.551

Melting Point: 2380 - 2420°C

II. LITERATURE REVIEW

A. Concept of an Active Powder

Gregg (1) was one of the first investigators to study the production of "active" powders by thermal decomposition of a parent substance from which a volatile product is released, as: Solid A → Solid B + Gas. The powder activity, although difficult to define precisely, reveals itself in such properties as: enhanced rate of reaction of the solid, increased rate of solution in solvents, and marked adsorptive capacity for gases. In general, two main factors are responsible for the phenomenon. One is the presence of an extensive "internal" area in the solid, so that it is essentially porous on the microscopic and molecular scale, and the other is the existence of lattice strain, so that some, or all, of the atoms or ions of the solid are displaced somewhat from the positions they would occupy in the perfect lattice. This term "strain" would include Frenkel or Schottky defects and dislocations as special cases. The internal area may arise in various ways. It may be due to the large volumes of channels of molecular size, left by the escaping gas in a framework of the remaining solid. More often, however, the area is due to the dispersed state of the solid which exists as crystallites, or micelles, of

small dimensions. The area thus produced may still be termed an internal area, since the micelles will aggregate to form grains visible to the naked eye.

The temperature at which bonding initially occurs can be considered a critical parameter of sintering. One of the easiest ways to lower this initiation temperature is by judicious control of the calcining cycle. It has been shown, by Hyde and Duckworth (2), that MgO obtained from the carbonate sinters at a much lower temperature if the calcination temperature is optimized beforehand. As seen in Figure 1, magnesium carbonate, which has been calcined at 1100°F and no higher, is, by far, the most sinterable of several calcines. This effect has been partially explained by Rosauer and Handy (3) whose investigations of the individual crystallite size in calcines of magnesium carbonate are given in Table 2. Note that the crystallite size grows rapidly at all temperatures. Apparently, the optimum amount of carbonate decomposition (enhancing sintering) and the minimum amount of crystallite growth (inhibiting sintering) occur at about 1100°F. Similar studies have been conducted on ThO_2 (4), Y_2O_3 (5), BeO (6), NiO (7), and MgO obtained from the hydroxide (8). All results indicate that there is some optimum calcination temperature for each particular compound.

TABLE 2.

Crystallite Sizes and Aggregate Sizes of MgO Calcines

Temperature (°C)	Crystallites (microns)	Aggregates (microns)
400	.004	3.73
600	.015	4.16
800	.072	4.34
1000	.143	4.90
1600	1.130	5.35
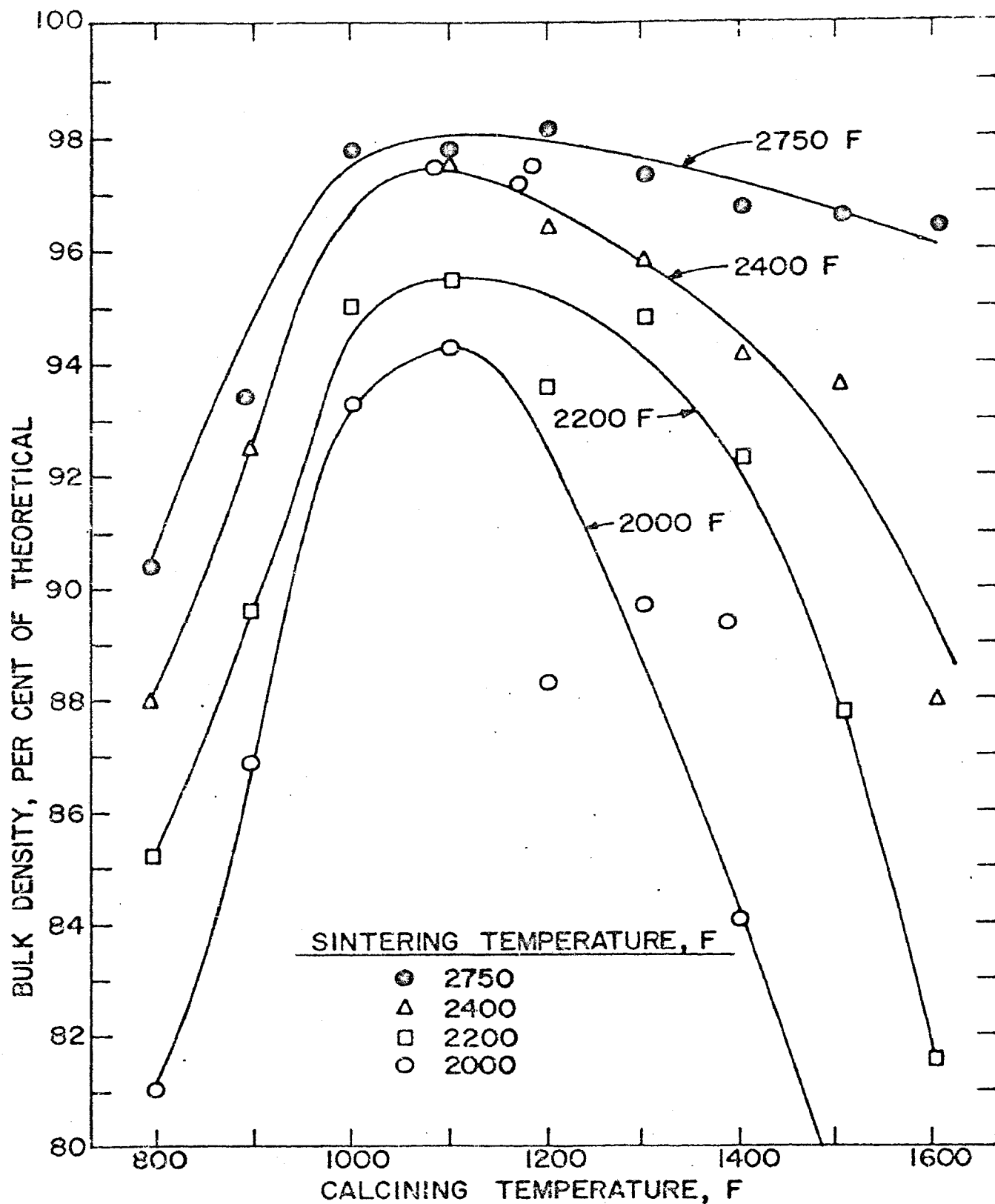
Figure 1.   Sintered Density of Magnesia Compacts
Prepared from Different Calcines.

B. Decomposition Process

The mechanisms of the thermal decomposition of solids are dominated by topochemical considerations. Thus the traditional concepts of order and molecularity, which play an important role in the kinetics of gas phase and liquid phase reactions, have little application in considerations of the kinetics of thermal decomposition of solids. Experimental observations of isothermal reactions are conveniently represented in the form of plots of fractional decomposition, α, versus time, t. The objective of any study of the thermal decomposition of a solid is usually the understanding of the mechanism of the chemical reaction. Such an idealized procedure is seldom realized in practice and one often has to be satisfied with an empirical analysis of the kinetics.

Although the general form of the $\alpha(t)$ curves can appear to vary from one reaction to the next, as shown by Jacobs and Tempkins (9), all these forms are special cases of the generalized decomposition curve shown in Figure 2. This curve exhibits an initial stage which occurs over ranges of α from 0.01 to 0.5. The gas evolution during phase I may be due to desorption of physically adsorbed gases or to a limited amount of thermal decomposition such as in a reaction which involves only a few atomic layers near the surface of the reactant. The extent of reaction during the induction
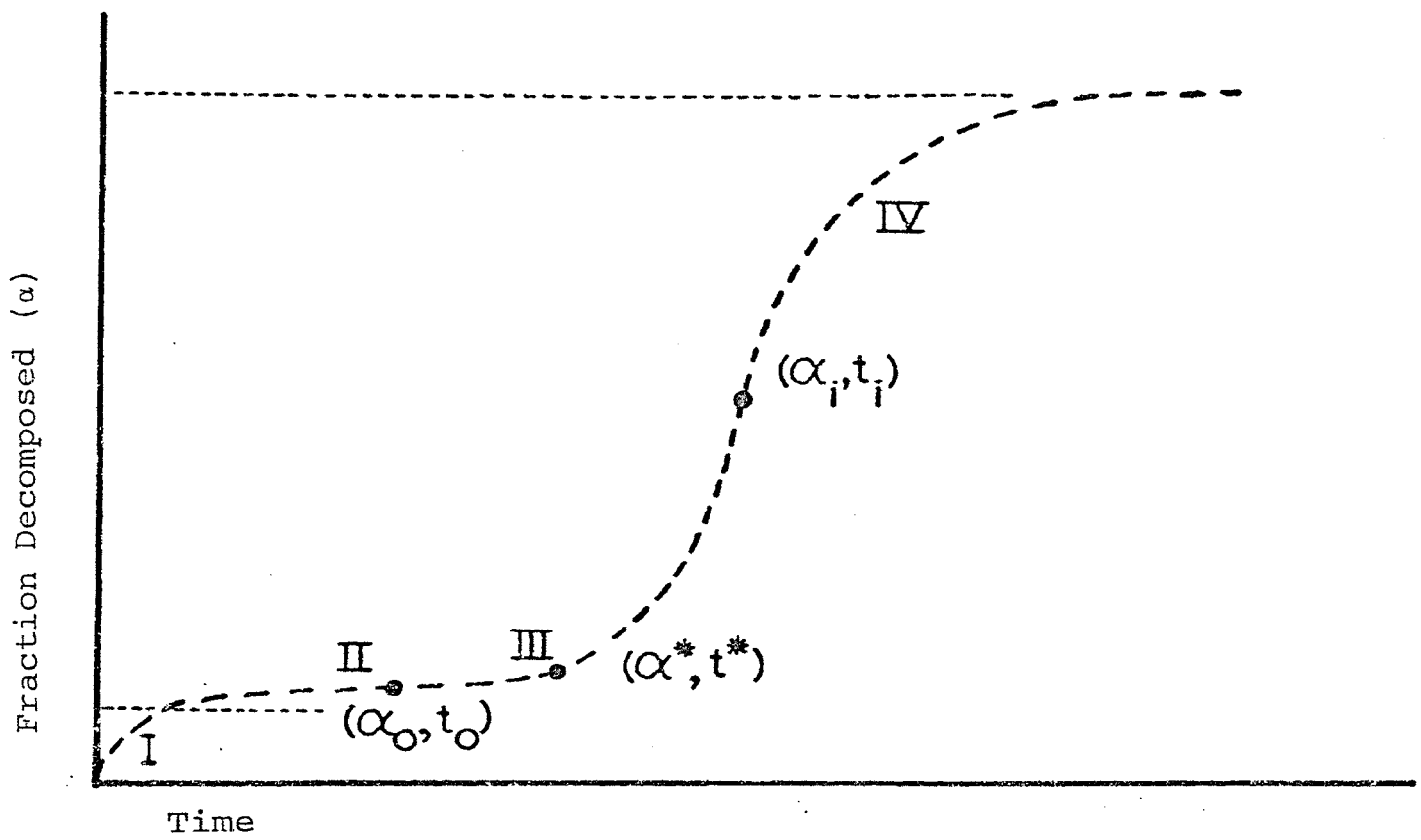
Figure 2.   General Decomposition Curve

period II is very limited, but after some critical time, t_o, the reaction rate increases rapidly during the acceleratory period III, finally reaching a maximum value at the point of inflection, t_i. For times greater than t_i, the reaction rate decreases steadily during period IV, finally falling to zero as the reaction ceases. The fractional decomposition at this stage may, or may not, correspond to almost complete decomposition of the starting material.

The above aspects of the kinetics of thermal decomposition can receive a formal explanation in terms of the concepts of the formation and growth of nuclei, as discussed by Langmuir (10). The essential basis of this theory is that a chemical reaction is confined to the interface between the solid reaction product and the undecomposed reactant. If the rate of this interface reaction is either constant, or a unique function of the area of the interface, then the kinetics of the reaction will be governed by the geometrical area of the interface. It is presumed that decomposition commences at certain selected points called nucleus forming sites.

Perhaps the most comprehensive treatment of the decomposition of solids in the form of powders is that of Mampel (11), who based it on two generalizations found by earlier investigators. One is that the rate of formation of nuclei follows a unimolecular law and the other is that the interface advances at a constant linear velocity. Considering

the powder is composed of a large number of isotropic spheres of radius, r, Mampel derived a general expression for the decomposition fraction. The expression reduces to simpler equations for three cases: (1) the induction period for which α is approximately proportional to the fourth power of time, i.e., $\alpha = kt^4$; (2) the intermediate period for which the equation, $(v/r)t = 1 - (1-\alpha)^{1/3}$, is a close approximation and (3) the final period in which the decomposition tends toward the unimolecular law, $\ln(1-\alpha) = kt +$ constant. For very fine powders, the decomposition follows the unimolecular law.

There have been many excellent articles on hydroxides or hydrated minerals which might provide some insight into the nature of the decomposition of chromium hydroxide. Brown, Clark and Elliott (12) have studied the decomposition of gibbsite, or alumina trihydrate. It was found that gibbsite could decompose either to the monohydrate, boehmite, or to chi-alumina which is virtually anhydrous. When the ignition temperature was raised, the decomposition of these two primary products followed independent routes, but these eventually led to a common product of alpha alumina at 1000°C. Eyraud, Goton and co-workers (13) found that after a short induction period, the rate of decomposition was constant at a given temperature to about $Al_2O_3 \cdot H_2O$, beyond which the rate diminished. From a plot of logarithm rate versus reciprocal of absolute temperature, an apparent

energy of activation of 31 k cal/mole was deduced.

The kinetics of decomposition of boehmite, $Al_2O_3 \cdot H_2O$, have been studied by Callister, Cutler and Gordon (14). A linear rate law was obeyed by the decomposition and an interface model was suggested as the mechanism of decomposition. The activation energy was 70 k cal/mole. The effect of water vapor on the rate of decomposition was observed. Kingery and Gordon (15) studied the decomposition of brucite, $Mg(OH)_2$, in vacuum. The brucite decomposed according to a first order rate equation consistent with a random nucleation process. Kinetic data for the decomposition of single crystals were more complex, but could be fitted to an interface model equation.

C. Characterization of Calcined Powders

Prior to 1950, the characterization of powders was commonly limited to information gained by particle size and surface area measurements, optical microscopy, X-ray diffraction and traditional chemical analysis. With increased emphasis on fine particles, usually in the context of high activity, more refined methods of characterization were applied, such as X-ray line broadening for crystallite size determination, spectrographic analysis and various absorption and exchange measurements which could be related to sintering activity. No longer is it sufficient to deduce mean crystallite sizes from X-ray line broadening. It is

necessary to see the ultimate particles and distinguish their nature at high magnification. The electron microscope has proven extremely valuable in this area.

While the majority of work on characterization of powders utilized magnesia (16), such oxides as alumina, beryllia and thoria have been studied by Murray (17). For MgO, BeO and ThO_2 decomposed in air, the process begins very rapidly at temperatures around 300°C. For probably all oxides, the individual crystallites are very closely joined to one another. Under conditions of processing at temperatures close to that of decomposition, the crystallites may be so weakly aggregated that virtually their whole surface area is available for gas adsorption.

Murray stated that electron microscopy observations on fine powders of MgO, BeO, and ThO_2 suggested that the crystallite shape in no case deviated markedly from an equiaxed form. Iwase, Takada and Hayashi (18) used electron microscopy and X-ray diffraction to study the calcination of metallic salts. The orientation of the resultant particles seemed to be greatly influenced by the pre-existing structure of the parent salts.

D. Sintering Process

Sintering may be defined as the mechanisms whereby a single pure material consolidates when subjected to external

influences of temperature, pressure and time insufficient to cause melting. The initial bond strength is increased by any factor that increases the packing density. As the temperature is increased, gases are released from the surface of the particles and bond strength increases slightly. As the temperature is raised higher, the contact area between particles increases as a result of surface forces promoting shrinkage. Toward the end of the sintering process, during which the voids close and the density increases, grain growth occurs and continues even after bulk shrinkage has ceased.

Four major modes of material transport have been suggested, and are shown in Figure 3. Any one of these may dominate under given conditions for a given material. Diffusion sintering models have been presented by Kuczynski (19), Cabrera (20), Herring (21), and Kingery and Berg (22). Volume diffusion is viewed as the transfer of atoms from the surface to the neck area, or, conversely, the migration of vacancies from the neck to the surface. However, the most important process is the migration of vacancies to grain boundaries. Material migrates from the grain boundaries to the neck area between particles with a resultant motion of the particle centers toward one another giving rise to a decrease in porosity.

Surface diffusion at free surfaces probably occurs in oxides at relatively low temperatures. However, the actual

Figure 3.

MATERIAL TRANSPORT MODELS
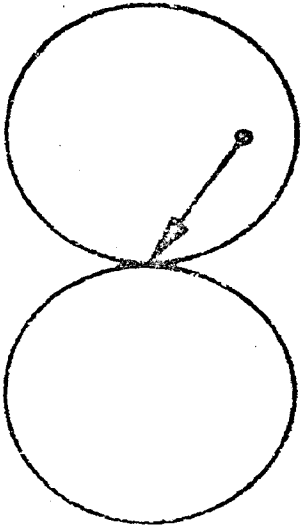
VOLUME DIFFUSION
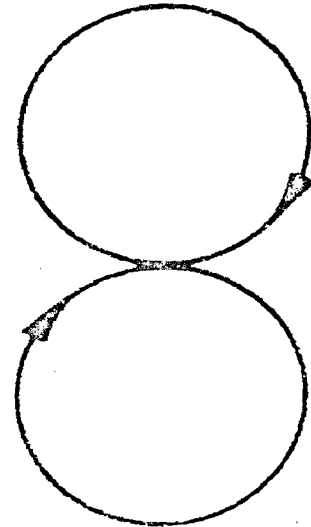
SURFACE DIFFUSION
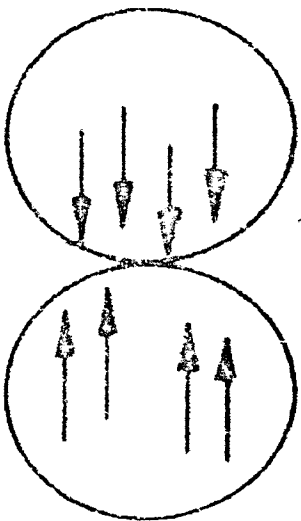
PLASTIC FLOW
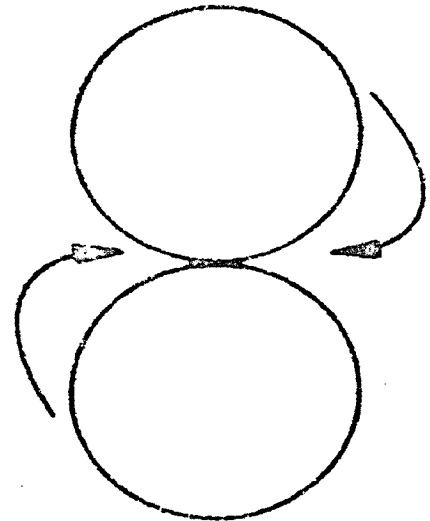
EVAPORATION AND CONDENSATION

number of mobile surface atoms is small and, therefore, transport of material by surface diffusion can not be very great. An evaporation and condensation mechanism is often dismissed as being too slow, or even inoperative, due to the low vapor pressure of refractory oxides. Due to the geometric effects of this mechanism, materials which exhibit a sufficiently high vapor pressure to evaporate, do not exhibit the shrinkage which is required for densification. However, this process is important for shrinkage since the competitive operation could reduce the available driving force under which shrinkage takes place. The mode of plastic flow is of importance in firing of ceramic materials in which the bond strength is due to the formation of a liquid phase. However, in the sintering of pure oxide ceramics, the formation of a liquid phase is avoided.

Although much work has been done on the sintering of chrome-magnesite refractories, it is only recently that investigators have studied sintering of pure Cr_2O_3. Hagel has conducted both cation (23) and anion (24) diffusion studies in Cr_2O_3, employing radioactive tracer techniques. His results showed that the difference between oxygen ion and cation diffusion coefficients is greater for Cr_2O_3 than for Al_2O_3 or Fe_2O_3. Oxygen diffusion in Cr_2O_3 is three to four orders of magnitude slower than chromium diffusion in the range 1100 to 1450°C.

Hagel, Jorgenson and Tomalin (25) studied the shrinkage rates of Cr_2O_3 prepared by thermal decomposition of $(NH_4)_2C_2O_7$. Results of these shrinkage curves indicate that the initial sintering of Cr_2O_3 can be described as a volume diffusion process where oxygen ions are the rate controlling species.

III. EXPERIMENTAL PROCEDURE

A. Decomposition

The decomposition of chromium hydroxide was studied using several of the techniques mentioned in the Introduction. The starting material was a $Cr(OH)_3$ gel, obtained from the Amend Drug and Chemical Company, New York, New York. Chromium hydroxide, according to several investigators (26,27), decomposes to form Cr_2O_3 at approximately 420°C. Samples of the hydroxide were heated at temperatures of 500, 600, 700, 800, 900 and 1000°C for periods of 1, 2, 4 and 8 hours. The samples were heat treated in Nichrome crucibles placed in a Kanthal-wound furnace. X-ray diffraction patterns were run on the parent gel and each sample following removal from the furnace.

The crystallite size of the resulting Cr_2O_3 powders was studied by the X-ray line broadening method, described by Klug and Alexander (28). A General Electric Model XRD-5 unit was used for all the X-ray work. The measurement taken in this technique is the width of an X-ray peak at one half its maximum intensity. This width increases with decreasing crystallite size below about 3000 Angstrom

units. An unbroadened peak is required for use as a reference so that the increase in width can be inserted into equation (1): $D = \frac{.9\lambda}{B COS\Theta}$, where D is the crystallite size in Angstrom units, λ is the radiation wavelength, Θ is one half of 2Θ (the peak angle) and B is the increased width of the peak in radians. An unbroadened peak was obtained from an X-ray pattern of a sample of $Cr(OH)_3$ heated at 1350°C for 24 hours. Several of the Cr_2O_3 peaks were studied to determine which would yield the best line broadening data. The Cr_2O_3 peak at 125.5° proved to be the most satisfactory peak.

There are numerous means of determining the degree of broadening from the X-ray patterns. The most accurate method appeared to be that of plotting 2Θ versus peak intensity at small increments over the complete peak. The goniometer was set at 0.05° intervals over the peak width and the intensity was recorded for 200-second periods. Background was determined by counting for the same period at each side of the peak and the average background was computed. This background was subtracted from the intensity measurements and the counts per second were plotted versus 2Θ. From this expanded profile, an accurate measurement of B was obtained. Figure 4 is an illustration of such a plot compared to that of the unbroadened peak. The value of B was obtained by subtracting b, the unbroadened breadth,
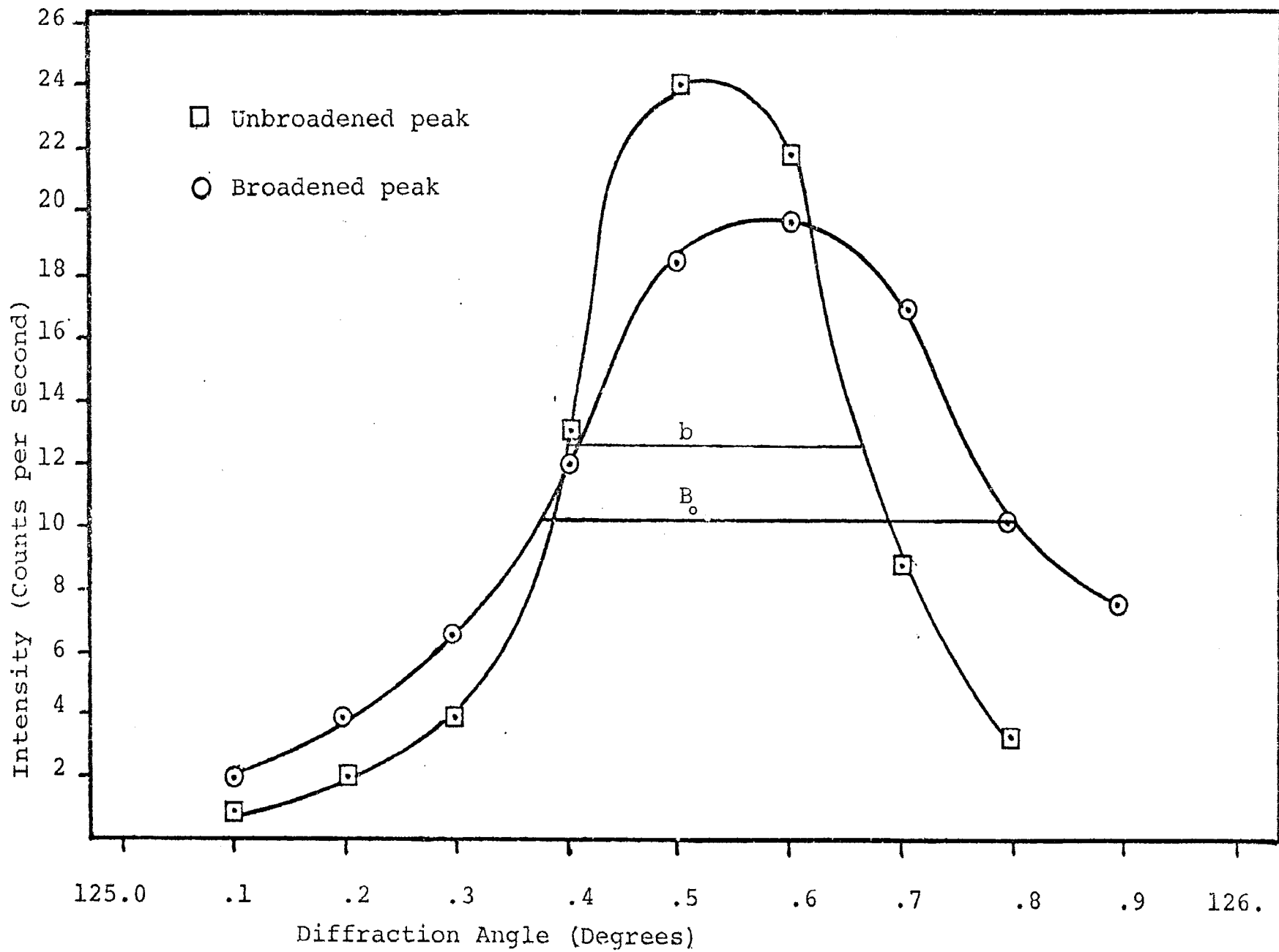
Figure 4. Comparison of Broadened and Unbroadened X-ray Peaks

from B_o, the broadened breadth. The crystallite size, D, was calculated by inserting the values of B into equation (1).

Particle sizes for the various calcines were determined by two methods. These data were obtained from both a Micromerograph apparatus and a Coulter Counter apparatus. The micromerograph, located at the U.S. Bureau of Mines, Metallurgy Research Center in Rolla, employs an air elutriation technique based on Stokes' Law to separate the various sizes of particles. The sample is de-agglomerated at the top of a seven-foot column, and allowed to fall downward against a flow of nitrogen onto a weigh balance. From a recording of weight versus time, the data can be converted into a weight fraction versus particle size plot. The Coulter Counter can be used to determine the number and size of particles suspended in an electrically conductive liquid by forcing the suspension to flow through a small aperture having an immersed electrode on either side. As a particle passes through the aperture it changes the resistance between the electrodes producing a voltage pulse having a magnitude proportional to the particle volume. The series of pulses is then electronically scaled and counted. By taking a series of counts at selected threshold levels, data are directly obtained for plotting cumulative frequency (larger than a stated

size) versus particle size. This principle does not permit discernment of particle shape and results are expressed in spherical equivalents. A typical calculation sheet is shown in Appendix A.

The most useful means of studying decomposition rates is by thermogravimetric analysis, that is, continuously monitoring the weight of a sample under thermal conditions. A number of weight loss studies were conducted using a Cahn Model RG electrobalance and a Texas Instruments Servo-Riter recorder in conjunction with a lab-constructed Kanthal-wound vertical furnace capable of being raised and lowered around the sample. A schematic diagram of this apparatus is shown in Figure 5. In these weight loss studies, it was convenient to express the degree of decomposition in terms of α, the fraction decomposed. Thus, a fraction of unity represents the maximum weight loss. In order to obtain decomposition rate data, the sample weight was monitored isothermally at several temperatures. To select these temperatures, it was necessary to run a temperature versus weight loss curve. This was done by placing a sample of the hydroxide in the furnace at room temperature and increasing the temperature at 20°C intervals, thus allowing the weight to equilibrate at each temperature.

The initial isothermal decomposition studies were conducted in atmospheres of ambient air. These studies

RECORDER

BALANCE CONTROL

BALANCE

FURNACE CONTROL

SUSPENSION WIRE

SAMPLE HOLDER

FURNACE (IN POSITION) (LOWERED)

THERMOCOUPLE
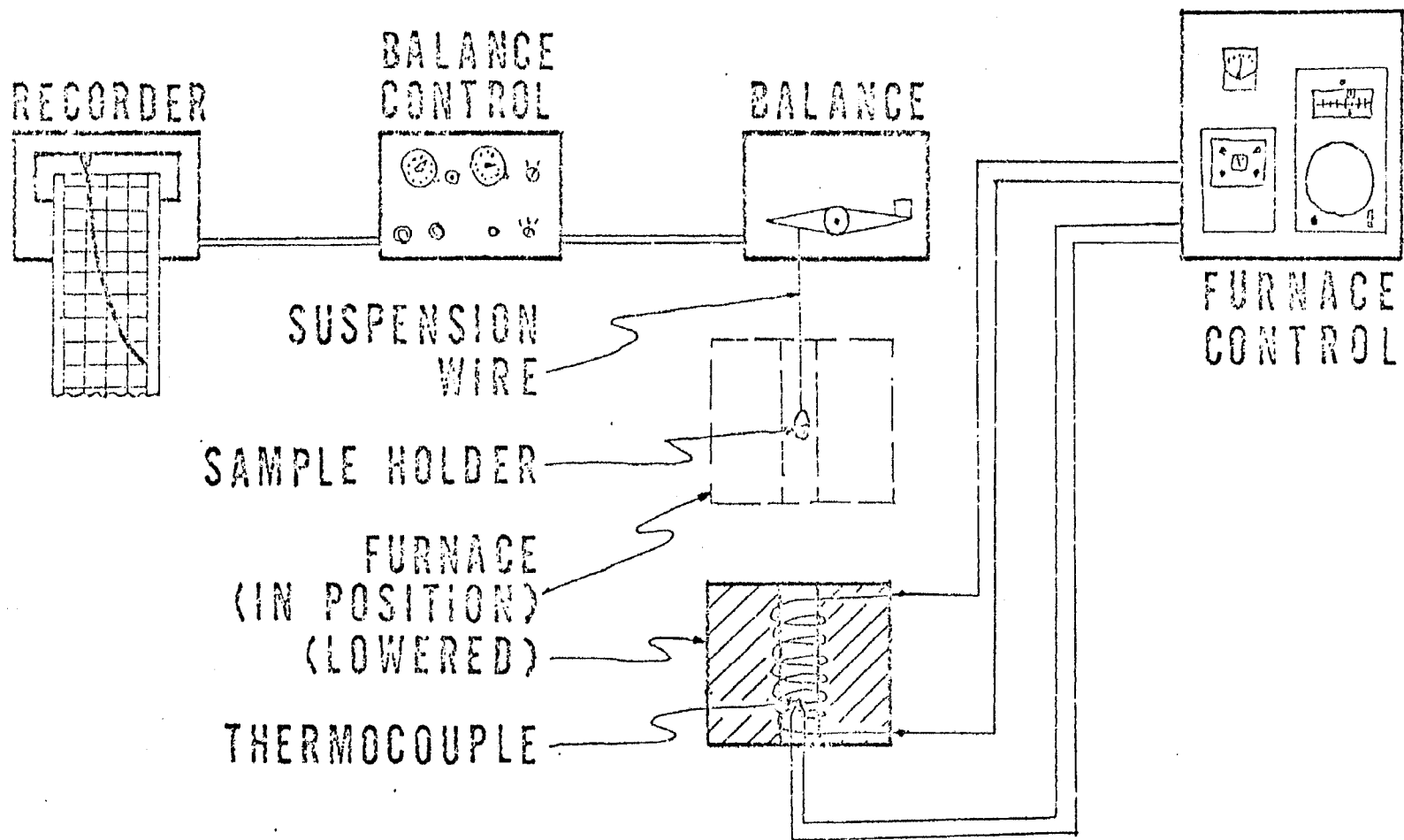
Figure 5.

TGA ASSEMBLY

were conducted on samples preheated to 350°C so that only the second weight loss step seen in the weight loss curve could be followed. Isothermal runs were made at temperatures of 440, 480, 520, 560 and 600°C. The sample was weighed on an analytical balance, suspended from the electrobalance and placed in the furnace at 350°C. Once the weight had decreased to a constant value, the furnace was removed and the temperature increased to the desired level. When this temperature was reached, the furnace was raised back into position and the weight loss monitored. The fraction decomposed was then plotted versus time for each temperature.

In order to study the decomposition under more controllable atmospheric conditions, studies were conducted under vacuum conditions following the method of Kingery and Gordon (15). In this case, an accessory to the electrobalance, a vacuum bottle, was utilized. A diagram of this experimental apparatus is shown in Figure 6. To this vacuum bottle were connected a Vycor hangdown tube for enclosing the sample, a vacuum line to a rotary pump and a thermocouple gauge for measuring pressure. The entire weighing mechanism was placed in the vacuum bottle and the electrical signals fed through vacuum connections. The procedure followed was to suspend the weighed sample in a small platinum bucket, zero the recorder and place the hangdown tube around the sample. The vacuum bottle was
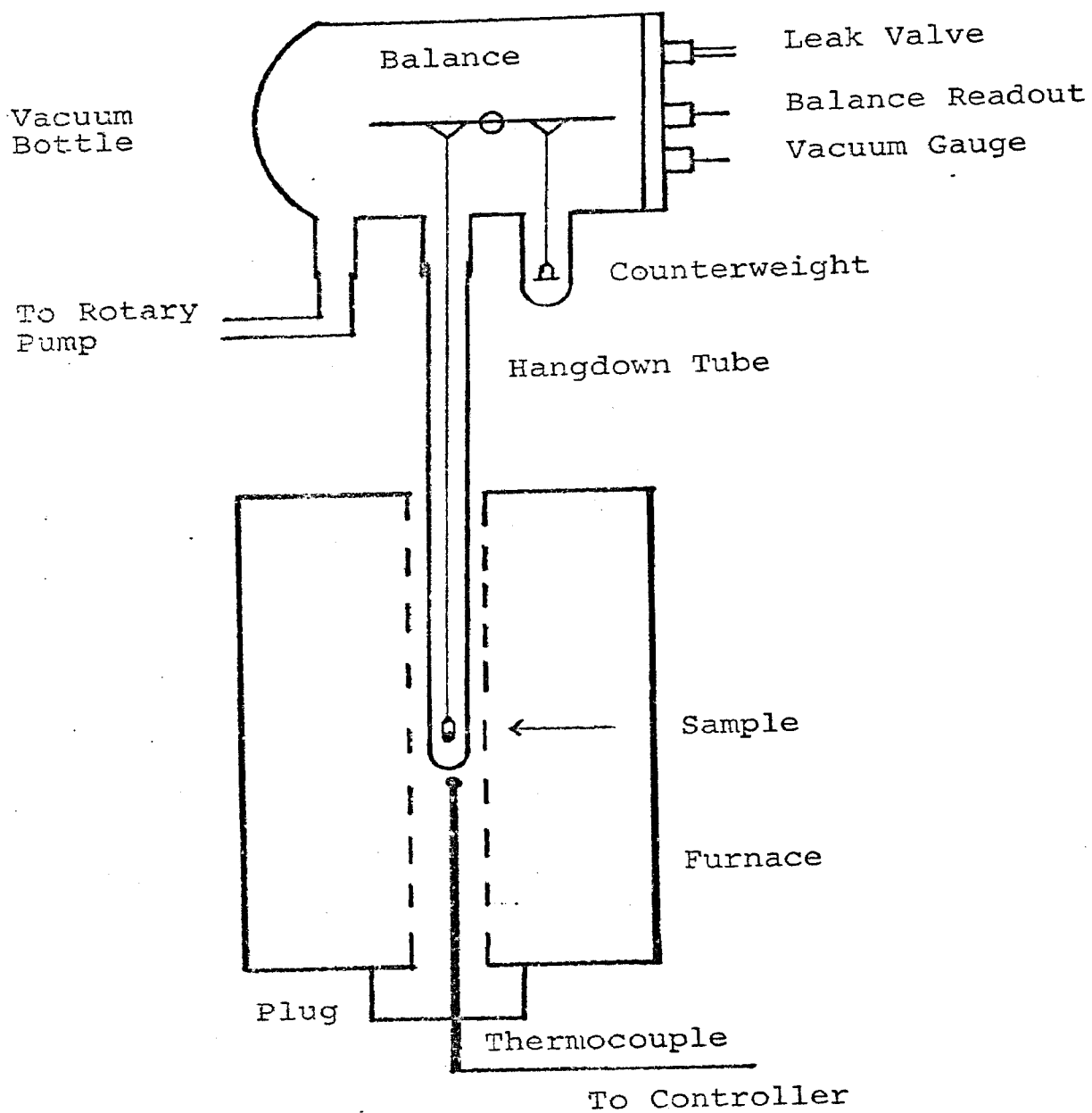
Figure 6. Diagram of Vacuum TGA

then evacuated to 100 microns of pressure and the weight recorded. Once the weight reached a constant value, the furnace, at the desired temperature, was raised around the sample and the weight loss recorded. Isothermal runs were made at temperatures from 380 to 500 degrees Centigrade. The fraction decomposed was then plotted versus time for each temperature.

Photographs of selected calcined powders were taken using both a Bausch and Lomb research metallograph and a Hitachi Model HU-11A electron microscope. The procedure followed with the metallograph was to place an acetone suspension of the powder on a cover glass slide and to allow the acetone to evaporate. Photomicrographs of the powders were then taken at a magnification of 500 times. For the electron microscope studies, a drop of a solution of collodion in amyl acetate was placed on the surface of distilled water. The electron microscope grids, mounted on a glass slide, were then used to pick up the thin film of dried collodion. A water suspension of the desired calcined powder was placed over the grid and allowed to dry. These grids were placed in the electron microscope and electron micrographs were taken at a magnification of 10,000 times.

Since the surface area of calcined powders is considered to be an indication of the activity of sinterable materials,

selected samples were sent to the seawater magnesia plant
of E. J. Lavino Refractories Company, where a Perkin-Elmer
Sorptometer was used to measure the surface areas. A
sample of the commercial gel and samples calcined for both
two and eight hours at 500, 600, 700, 800, 900 and 1000°C
were tested.

B. Sintering

The sintering behavior of chromium oxide powders,
produced by the calcination of chromium hydroxide, was
studied by forming pellets of the powders and firing
these at elevated temperatures. Pellets of powders
calcined for two hours at 400, 500, 600, 700, 800 and
900°C were formed by pressing the powders in a one-half
inch diameter die. The pellets were fired at temperatures
of 1500, 1600, 1700 and 1750°C under ambient air atmosphere.
In order to study the effect of atmosphere upon sintering,
identical pellets were fired in flowing oxygen and nitrogen
atmospheres at temperatures of 1500, 1600, and 1700°C.
All the pellets were fired in a platinum-wound furnace
manufactured by Engelhard Industries. The pellets were
placed in the furnace at room temperature, the temperature
raised to the desired level and maintained there for 12 hours,
after which the furnace was allowed to cool naturally.

Density measurements were taken on the fired pellets
by measuring the dry weight and the saturated and suspended

weights after being immersed in boiling water for two hours. These values were inserted into the equation, apparent density equals dry weight/saturated weight-suspended weight, and the densities calculated. The pellets were then mounted in Bakelite, ground on 240, 320 and 600 grit grinding paper and polished with a slurry of one micron alumina polishing compound. Photo-micrographs of the microstructures were taken on a Bausch and Lomb metallograph at a magnification of 250 times.

IV. PRESENTATION OF RESULTS

The results of the X-ray line broadening data are shown in Figure 7 as a log-log plot of crystallite size versus time at 700, 800, 900 and 1000°C. Plotting the logarithm of the crystallite growth rate versus the reciprocals of the absolute temperatures yields the Arrhenius plot seen in Figure 8.

The particle size distribution plots for selected calcined samples are shown in Appendices B and C, for the Coulter Counter and Micromerograph data, respectively. Figure 9 shows the results of the surface area measurements for samples calcined for both two and eight-hour periods. Table 3 presents values for: 1) the crystallite diameter in Angstrom units, 2) the median particle sizes in microns, and 3) the surface areas in square meters per gram for selected calcined samples.

Figure 10 is a weight loss versus temperature curve for the $Cr(OH)_3$ under ambient atmospheric conditions. The isothermal decomposition plots at 440, 480, 520, 560 and 600°C, under ambient atmospheres, are seen in Figure 11.

Figure 12 is a weight loss versus temperature curve for the $Cr(OH)_3$ under vacuum at 100 microns pressure. The

initial portions of the isothermal decomposition plots at 410, 440 and 470°C under vacuum are shown in Figure 13. Plotting the logarithm of the decomposition rates versus the reciprocals of the absolute temperature yields the Arrhenius plot as seen in Figure 14. The decay portions of the decomposition curves of $Cr(OH)_3$ at 380, 410, 440, 470 and 500°C are shown in Figure 15. A test for first-order kinetics is shown by plotting log $(1-\alpha)$ versus time for the decay portion of these decomposition curves in Figure 16.

Photomicrographs of the hydroxide calcined for two and eight hours at 600 and 900°C are shown in Figures 17 through 20. Electron micrographs of samples calcined for two and eight hours at 500, 600, 700, 800 and 900°C are shown in Figures 21 through 30. Figure 31 is an electron micrograph of the parent gel, and Figure 32 is an electron diffraction pattern obtained from a sample calcined for eight hours at 900°C.

The results of the sintering studies are shown in the next three figures. The densities of pellets fired in air, oxygen and nitrogen atmospheres are plotted versus the calcining temperatures in Figures 33, 34 and 35, respectively. Photomicrographs of pellets fired in air at 1700°C are shown in Figures 36 through 38; photomicrographs of pellets fired in oxygen are shown in Figures 39 through 41, and photomicrographs of pellets fired in nitrogen are shown in Figures 42 through 44.
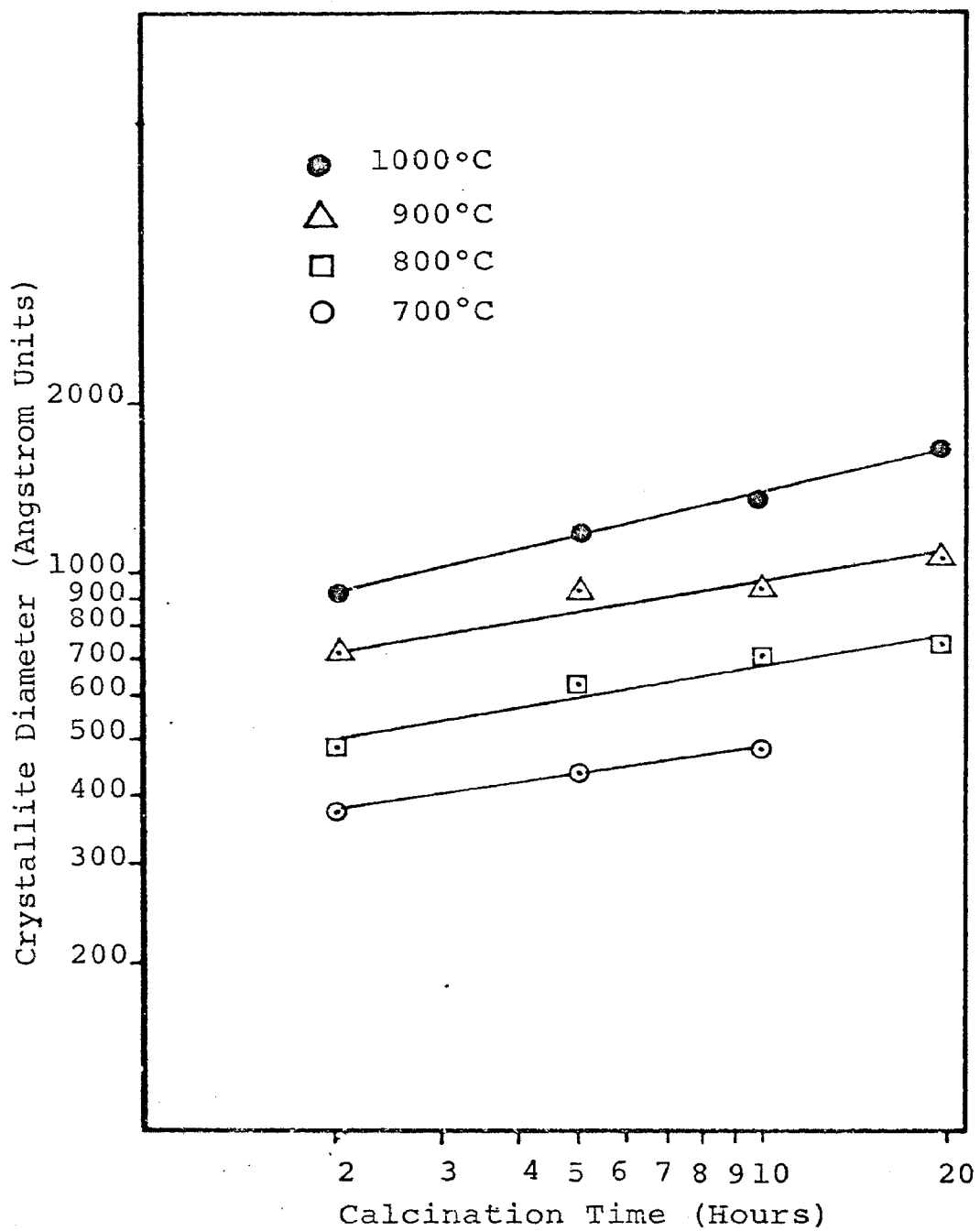
Figure 7. Growth Rate Plots for Crystallites
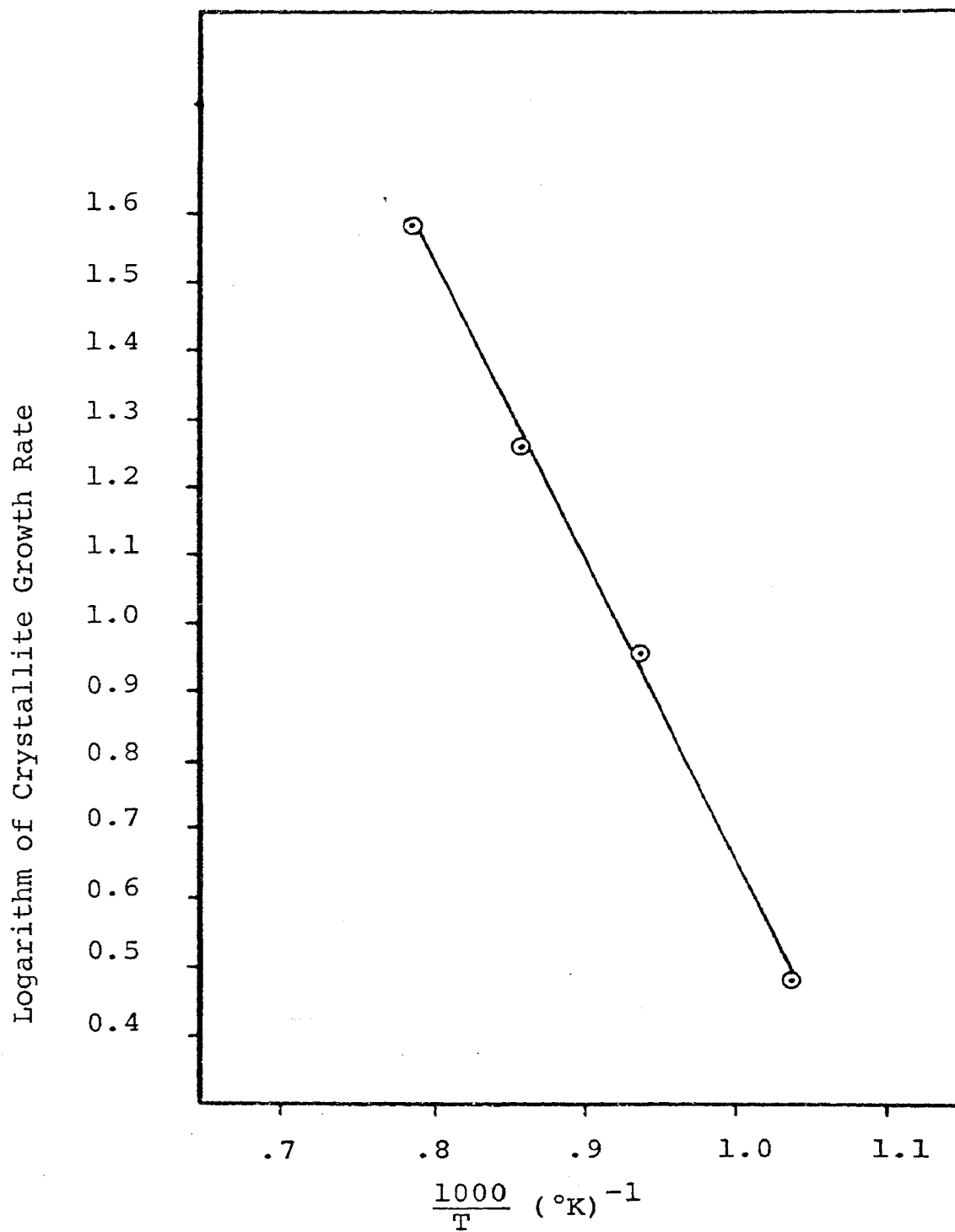
Figure 8.   Arrhenius Plot for Crystallite
Growth
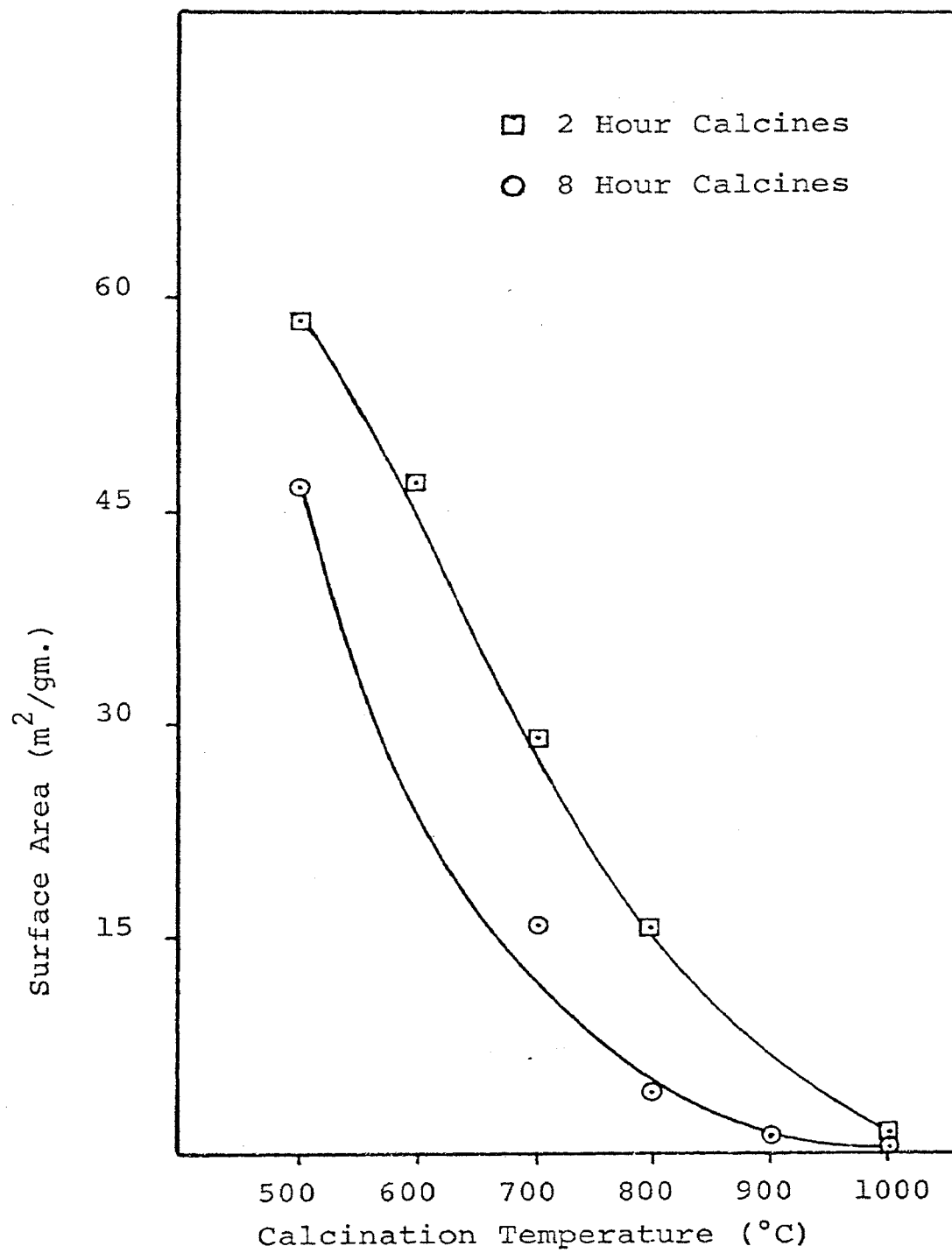
Figure 9. Surface Areas of Various Calcines

TABLE 3.

Crystallite Sizes, Particle Sizes and Surface
Areas of Cr_2O_3 Calcines

Sample	Crystallite Size (Angstrom units)	Median Particle Size (microns)		Surface Area $(m^2/gm.)$
		A	B	
gel	---	3.9	---	195.4
500-2	---	---	---	57.9
600-2	---	3.3	5.8	47.5
700-2	375	---	---	27.9
800-2	480	---	7.9	14.9
900-2	740	---	---	---
1000-2	905	4.2	8.2	.97
500-8	---	3.5	4.9	47.4
600-8	---	3.6	7.0	---
700-8	400	4.6	8.0	15.4
800-8	650	---	---	4.10
900-8	950	5.0	8.2	1.03
1000-8	1250	5.2	8.2	.82

A)   Micromerograph data

B)   Coulter Counter data
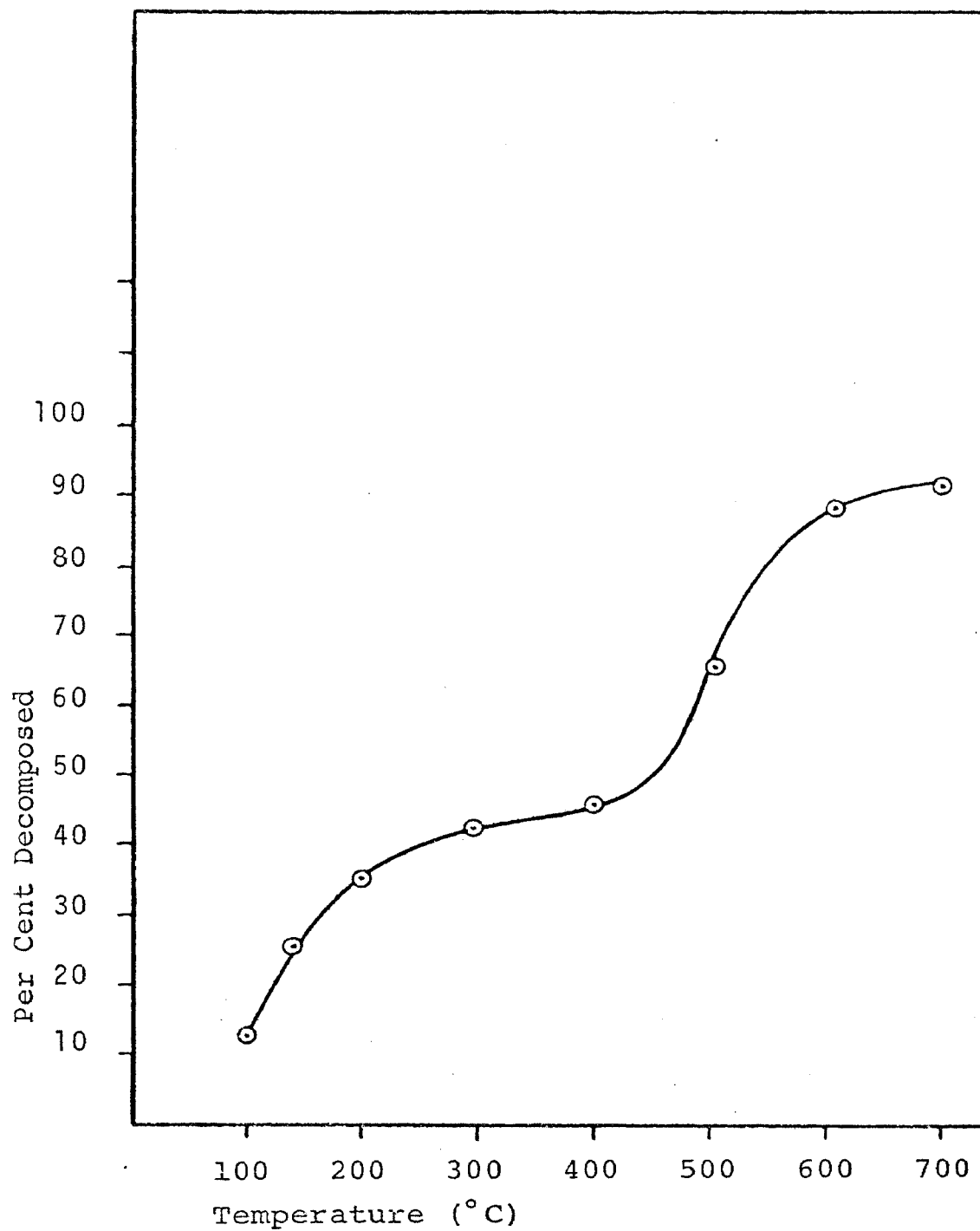
Figure 10. Weight Loss Curve Under Ambient
Atmospheres
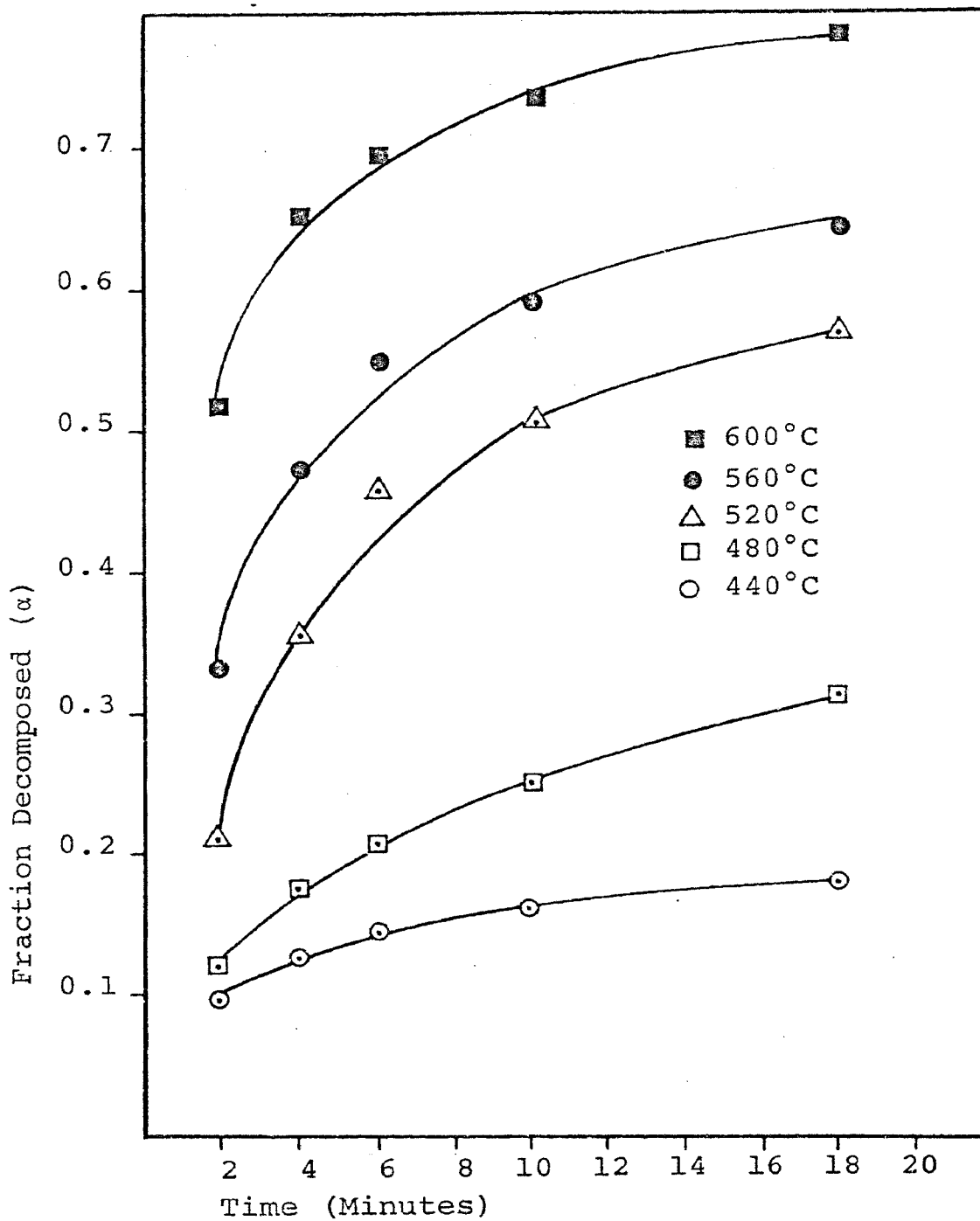
Figure 11. Decomposition Plots Under Ambient Atmospheres
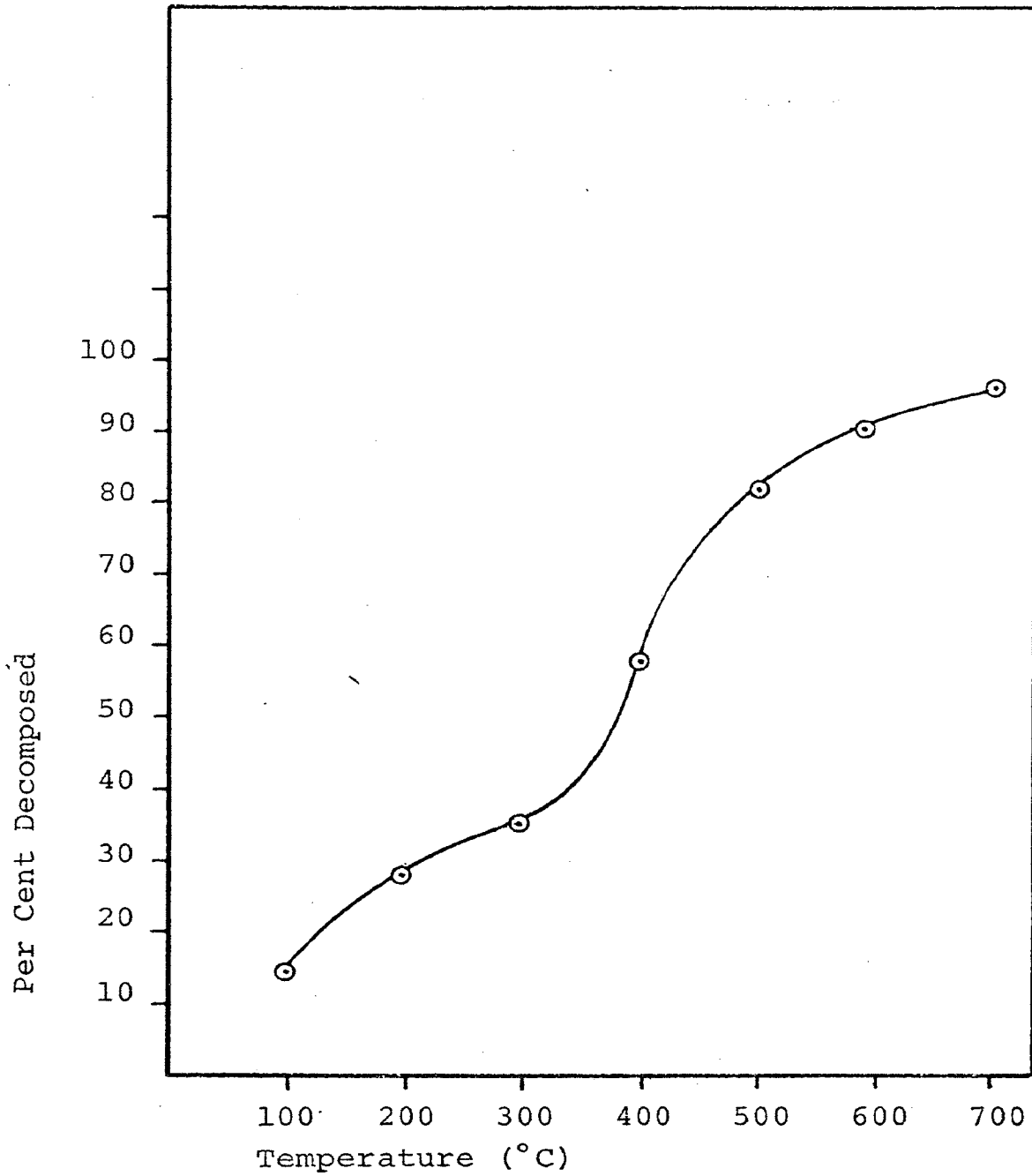
Figure 12.   Weight Loss Curve Under Vacuum
Conditions
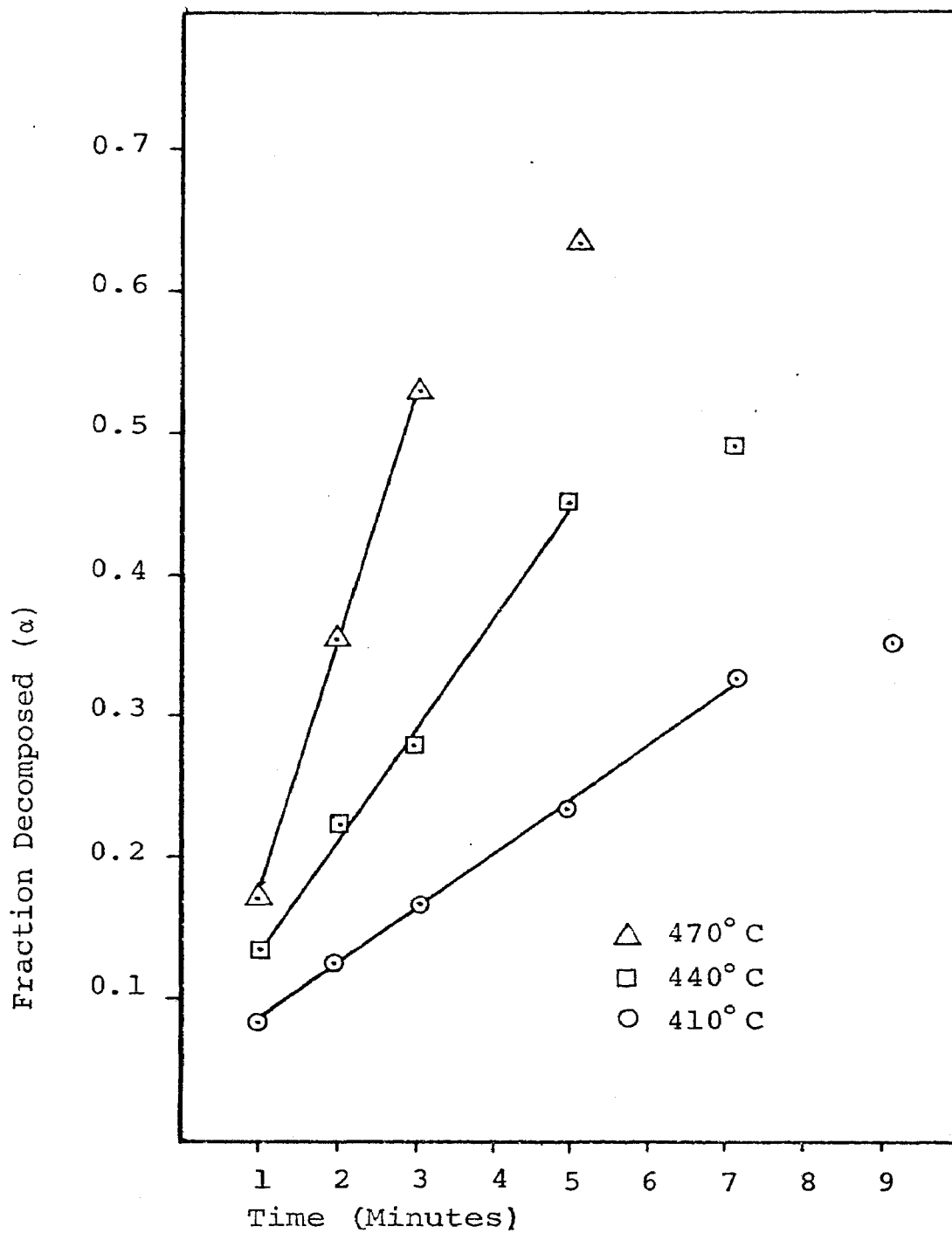
Figure 13. Decomposition Plots for Acceleratory
Region Under Vacuum Conditions
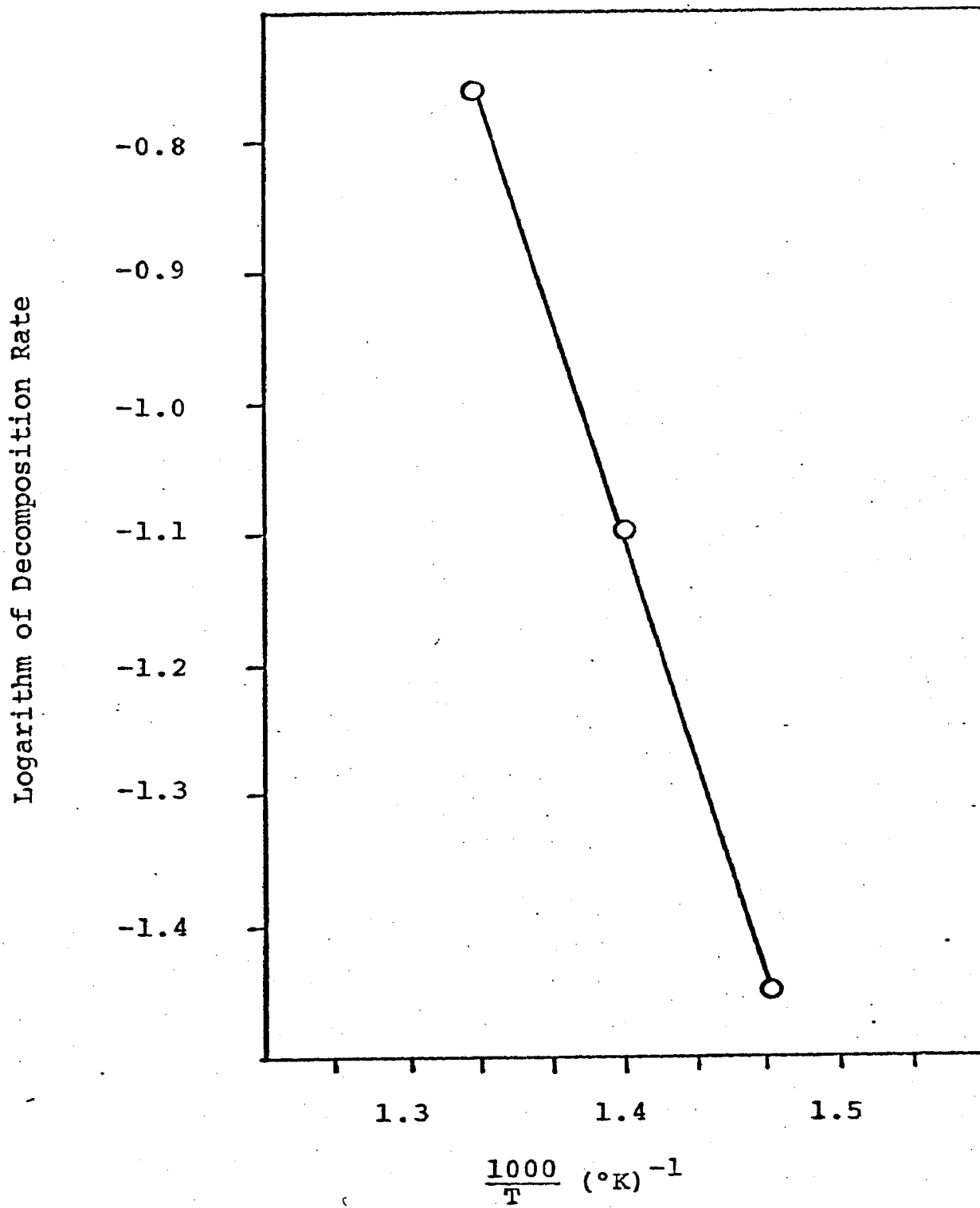
Figure 14.   Arrhenius Plot for Decomposition Under Vacuum Conditions
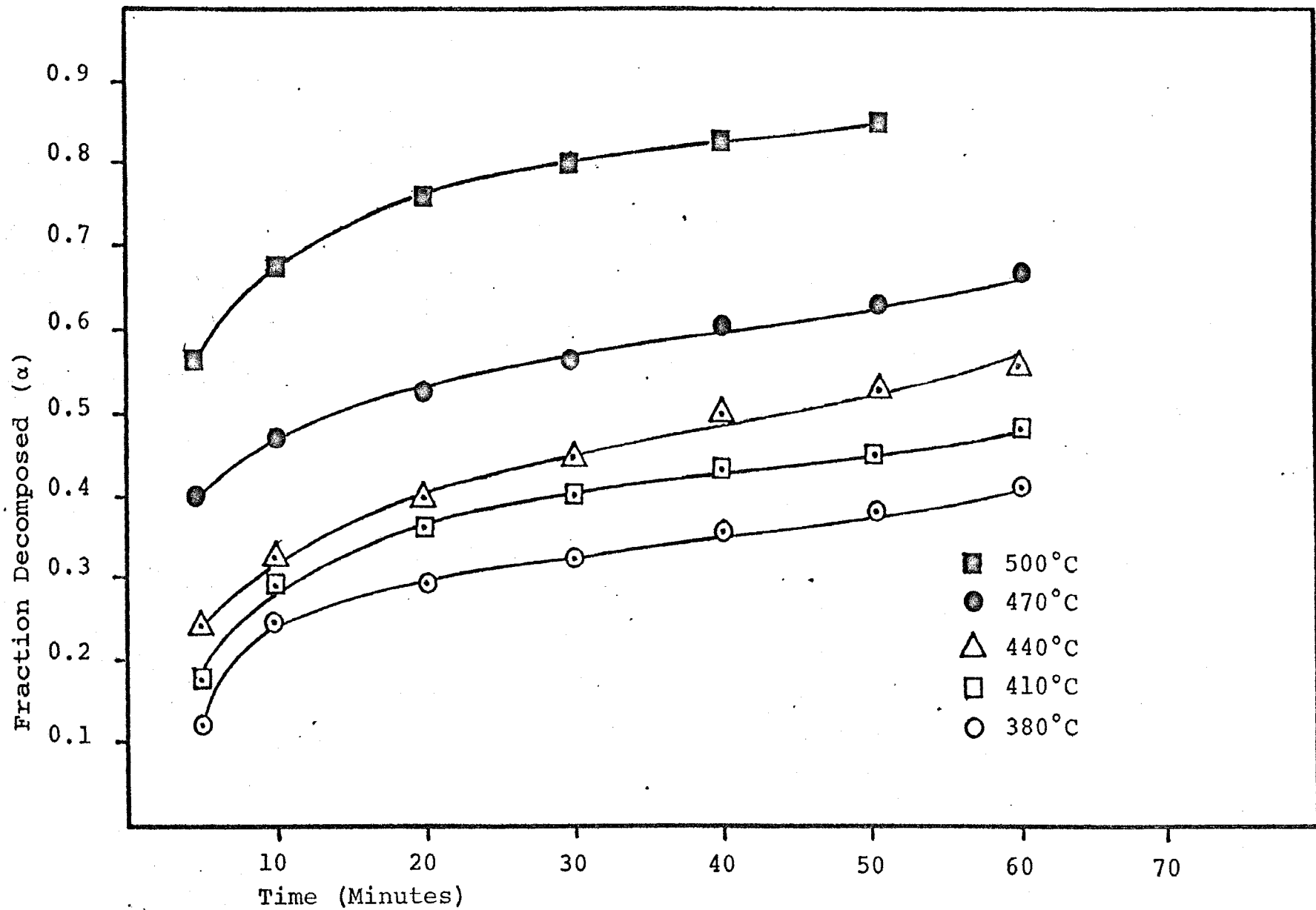
Figure 15. Decomposition Plots for Decay Region Under Vacuum Conditions
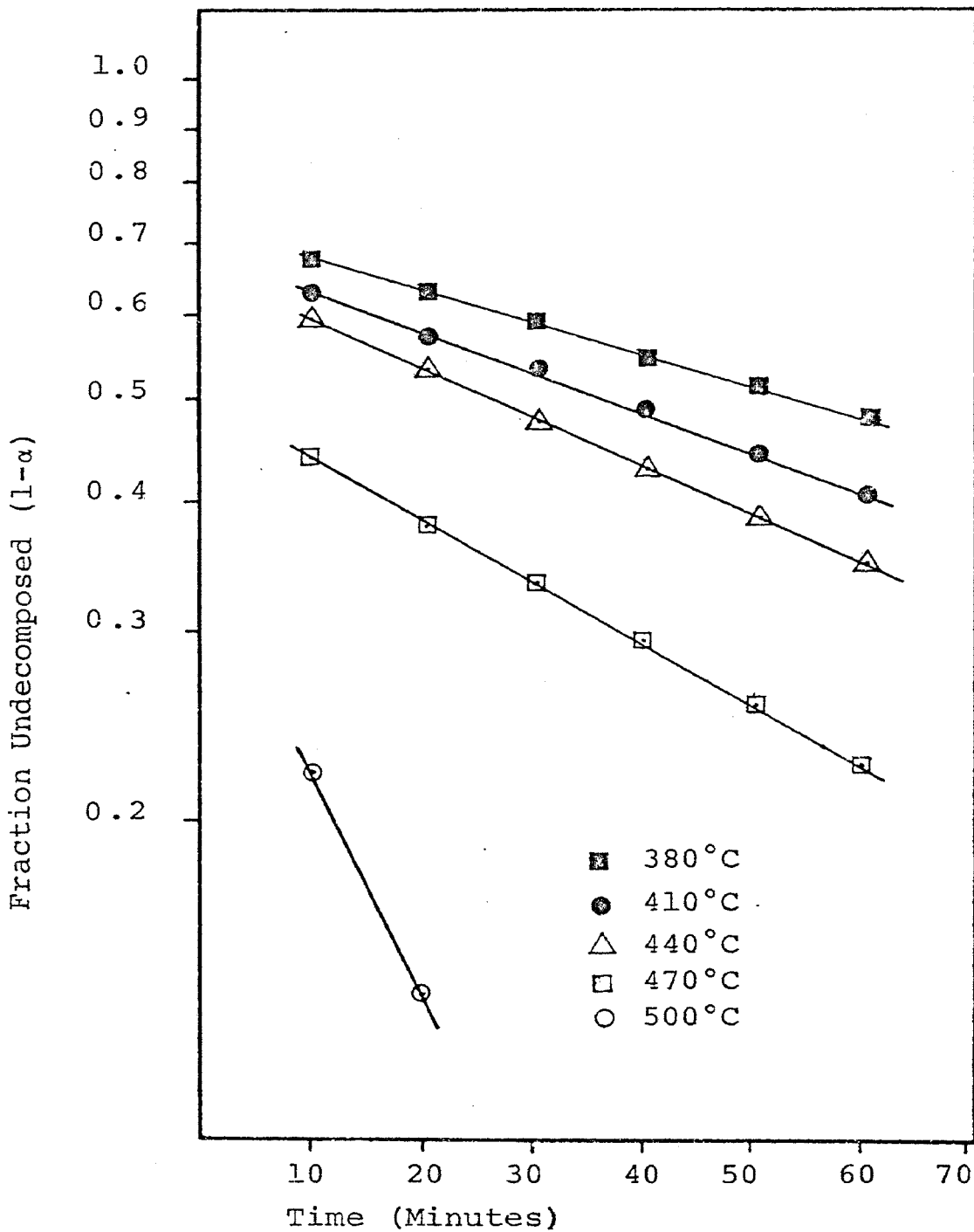
Figure 16.   Test for First Order Kinetics
of Decomposition
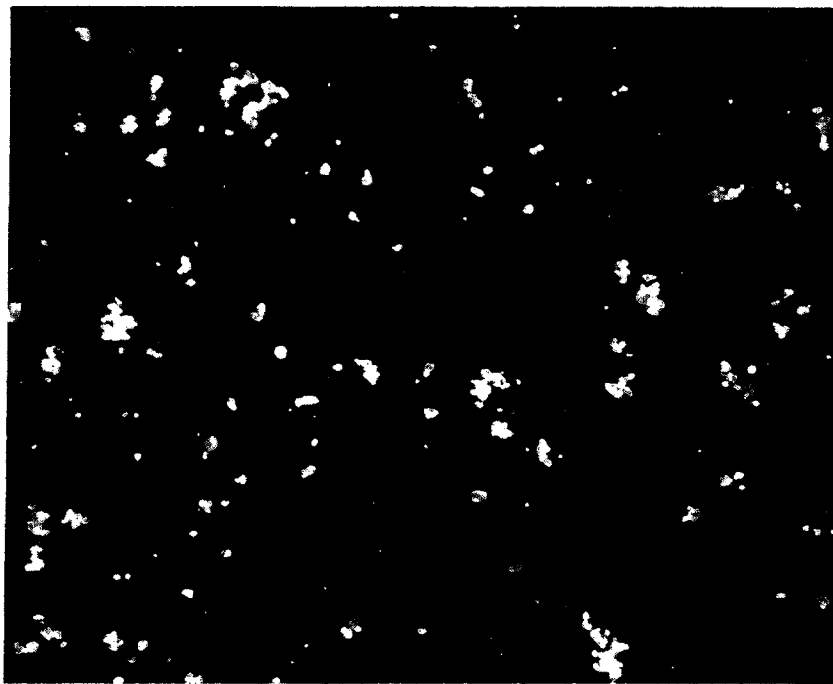
Figure 17. Photomicrograph of Sample Calcined 2 Hours at 600°C
           (500X)
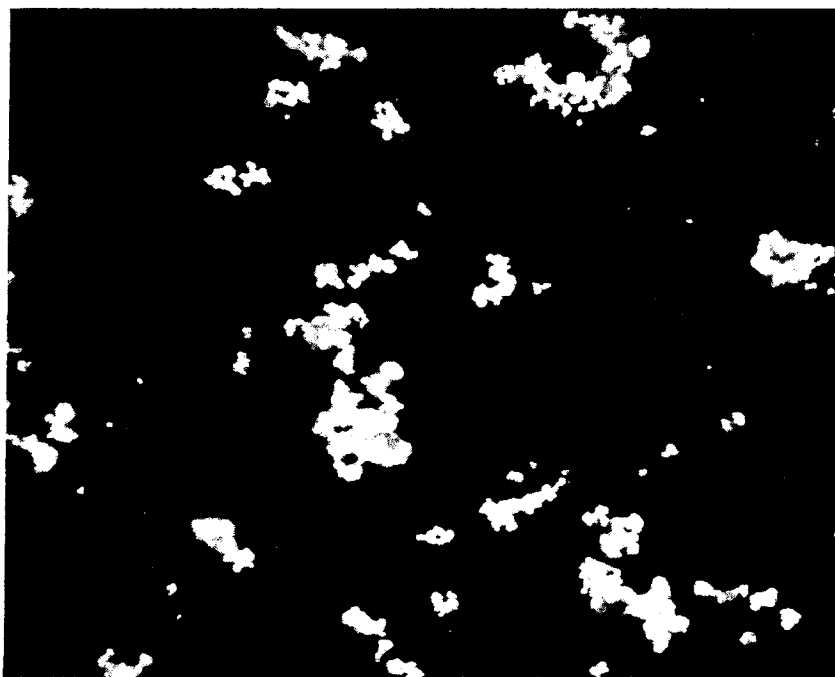
Figure 18. Photomicrograph of Sample Calcined 8 Hours at 600°C
           (500X)
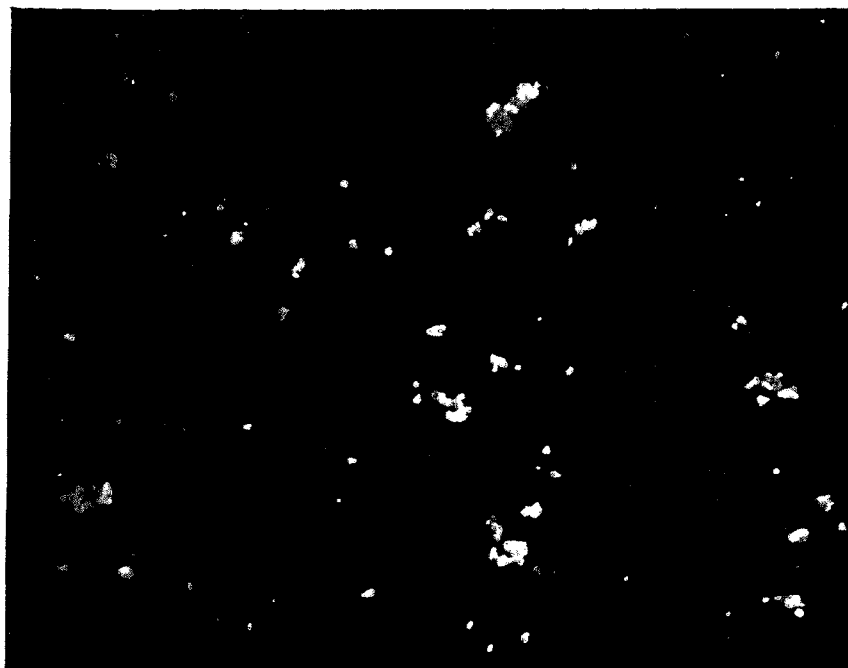
Figure 19.   Photomicrograph of Sample Calcined 2 Hours at 900°C
            (500X)
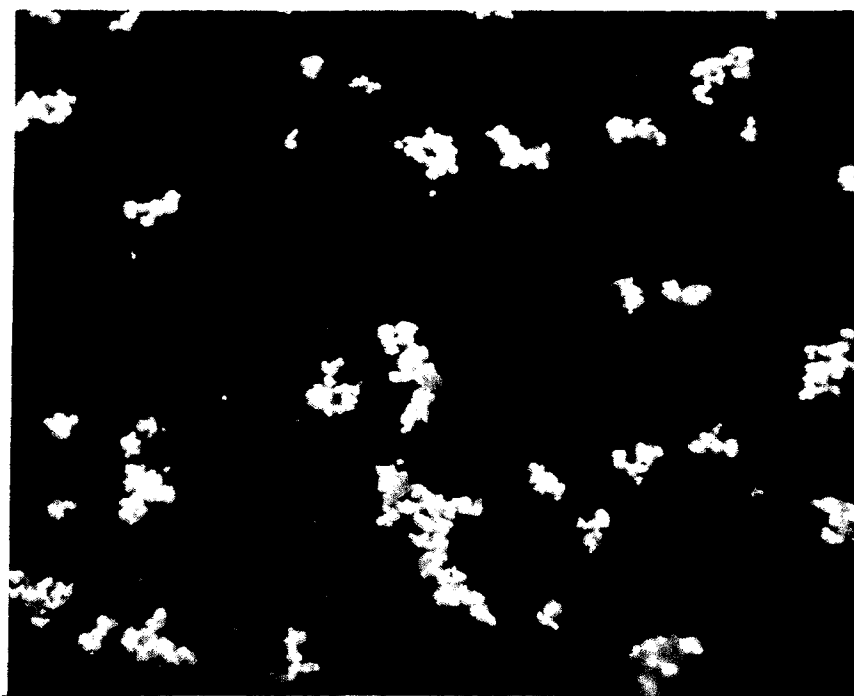
Figure 20.   Photomicrograph of Sample Calcined 8 Hours at 900°C
            (500X)
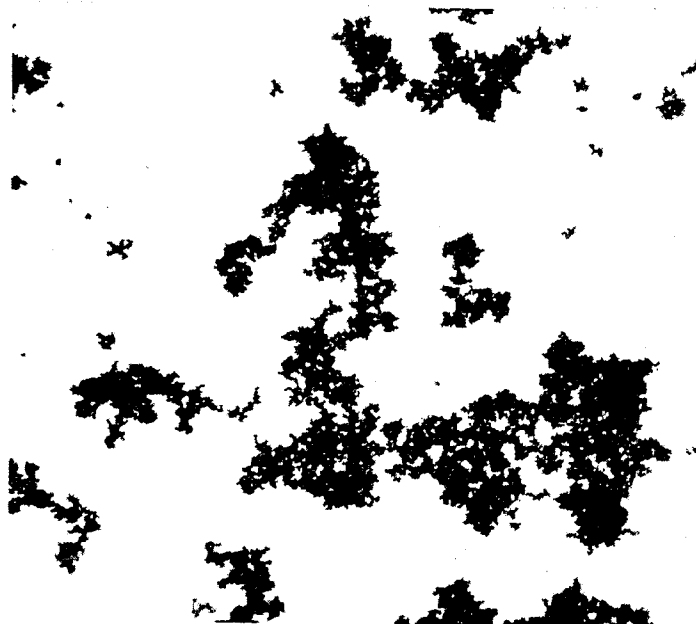
Figure 21. Electron Micrograph of Sample Calcined 2 Hours at 500°C
(10,000X)
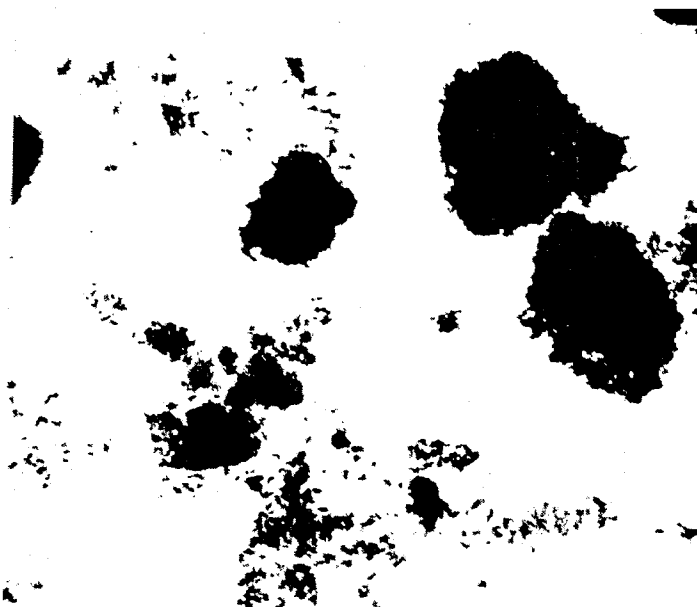
Figure 22. Electron Micrograph of Sample Calcined 2 Hours at 600°C
(10,000X)
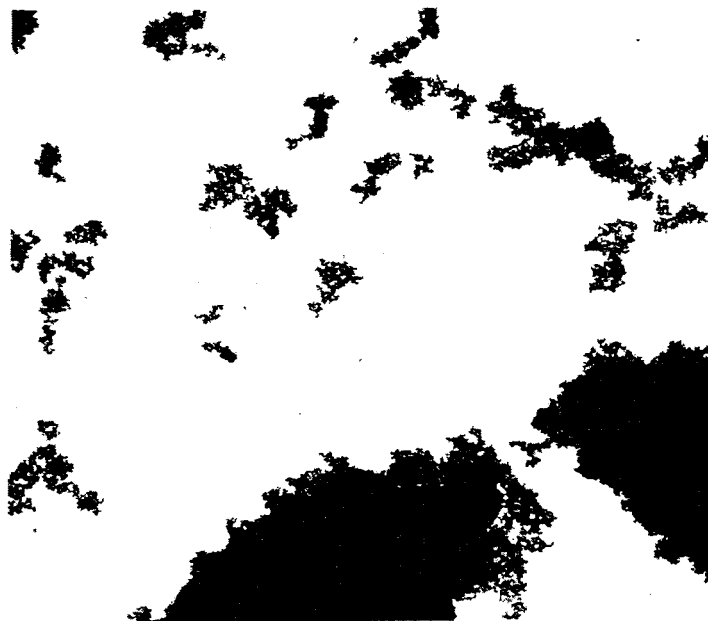
Figure 23. Electron Micrograph of Sample Calcined 2 Hours at 700°C
(10,000X)
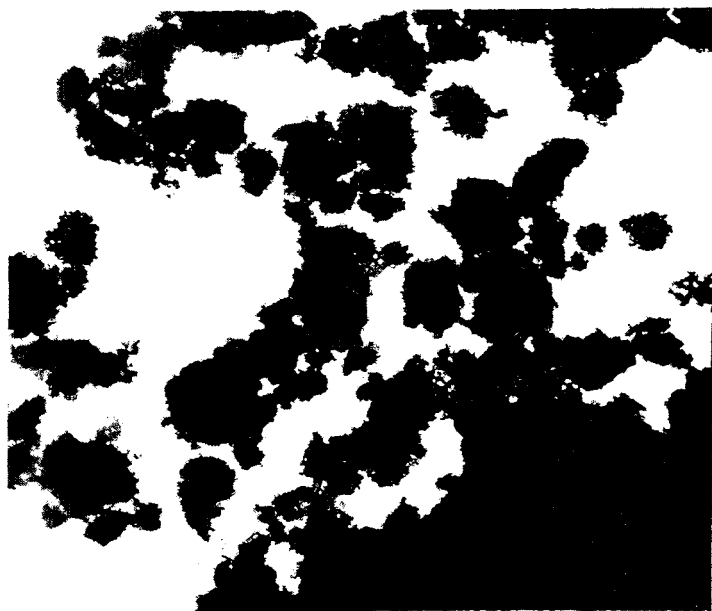
Figure 24. Electron Micrograph of Sample Calcined 2 Hours at 800°C
(10,000X)
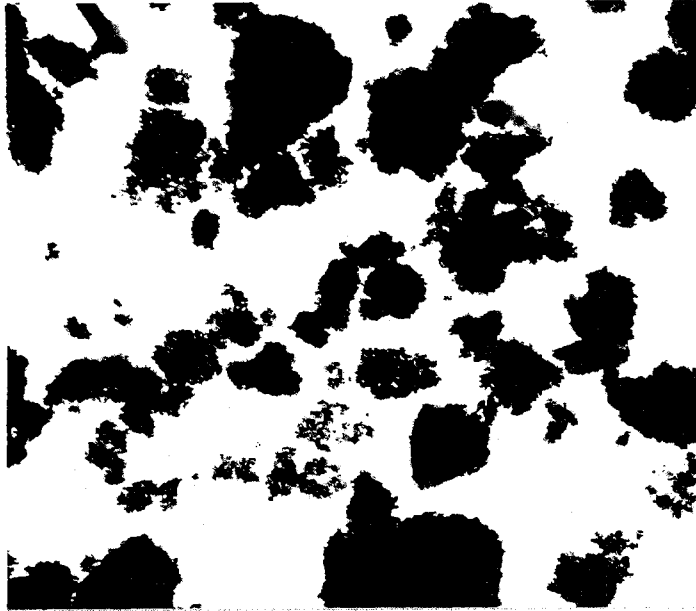
Figure 25.   Electron Micrograph of Sample Calcined 2 Hours at 900°C
             (10,000X)
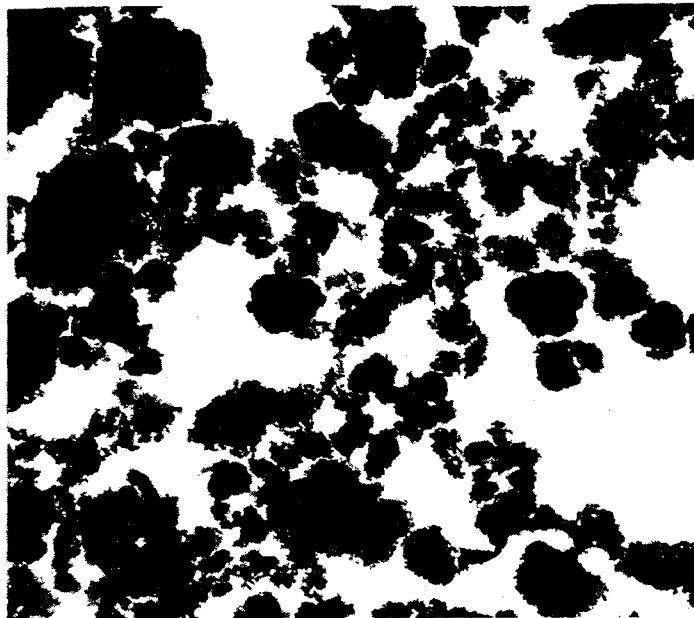
Figure 26.   Electron Micrograph of Sample Calcined 8 Hours at 500°C
             (10,000X)
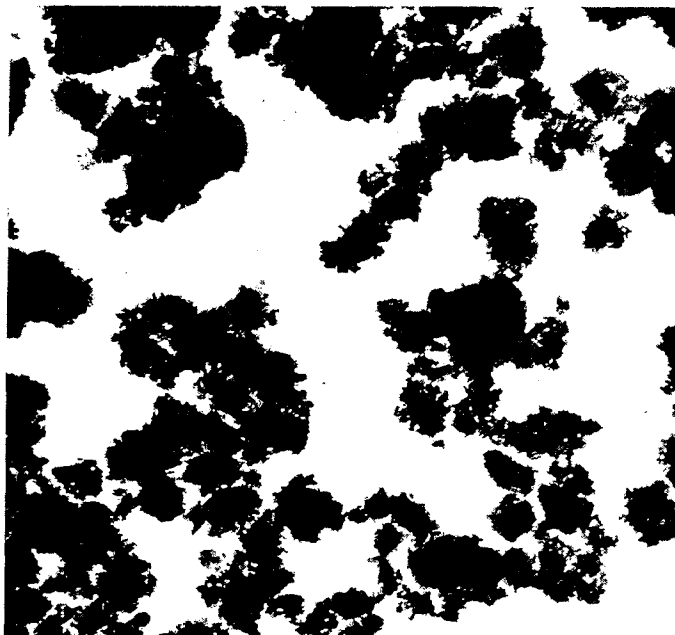
Figure 27. Electron Micrograph of Sample Calcined 8 Hours at 600°C (10,000X)

Figure 28. Electron Micrograph of Sample Calcined 8 Hours at 700°C (10,000X)

48

Figure 29.   Electron Micrograph of Sample Calcined 8 Hours at 700°C
             (10,000X)

Figure 30.   Electron Micrograph of Sample Calcined 8 Hours at 900°C
             (10,000X)
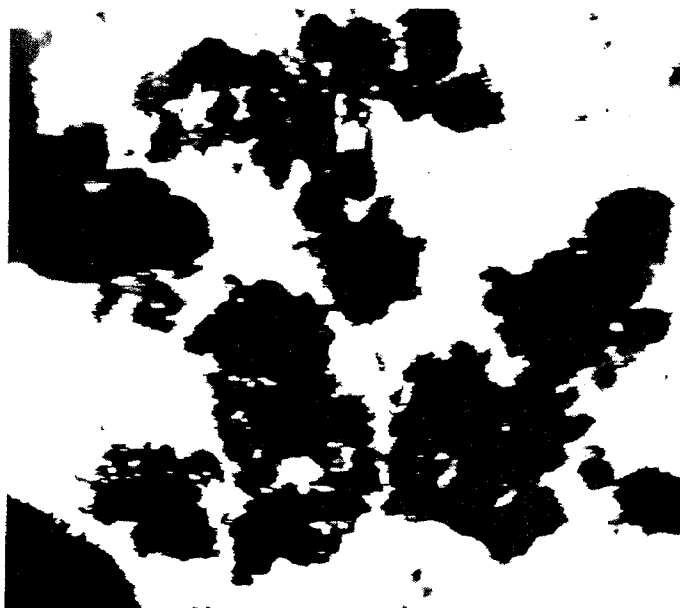
Figure 31.   Electron Micrograph of Hydroxide Gel Sample
(10,000X)
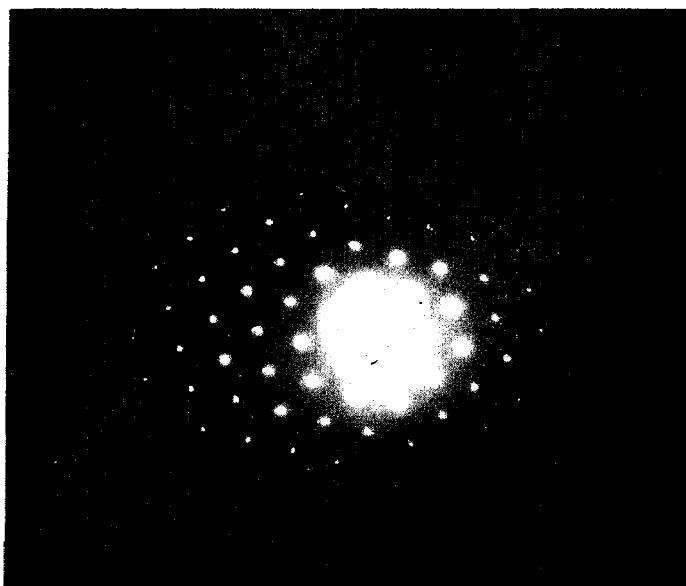
Figure 32.   Electron Diffraction Pattern Obtained from Sample
Calcined 8 Hours at 900°C
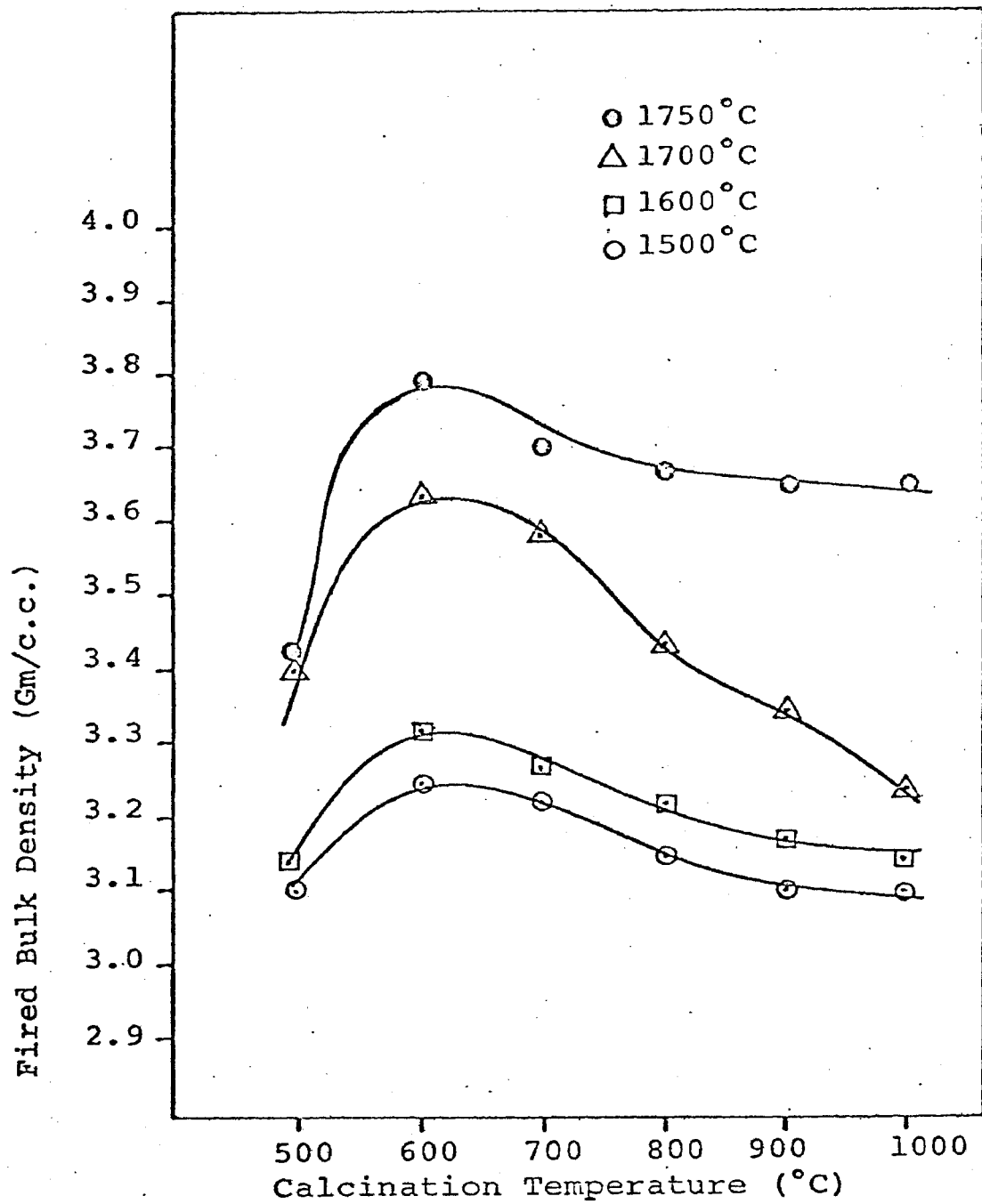
Figure 33. Densities of Cr_2O_3 Pellets
Fired in Air Atmosphere
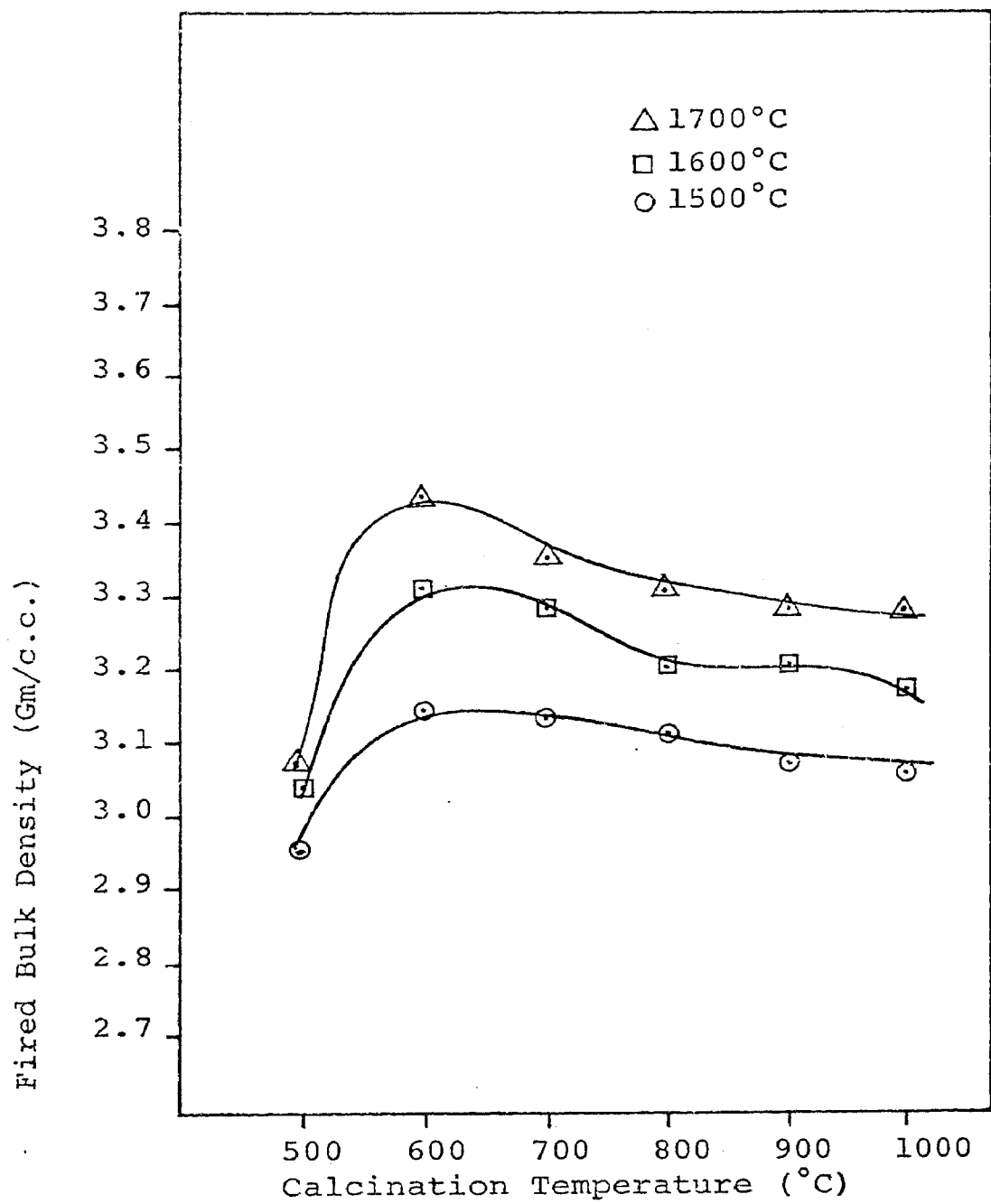
Figure 34.   Densities of Cr_2O_3 Pellets
            Fired in Oxygen Atmosphere
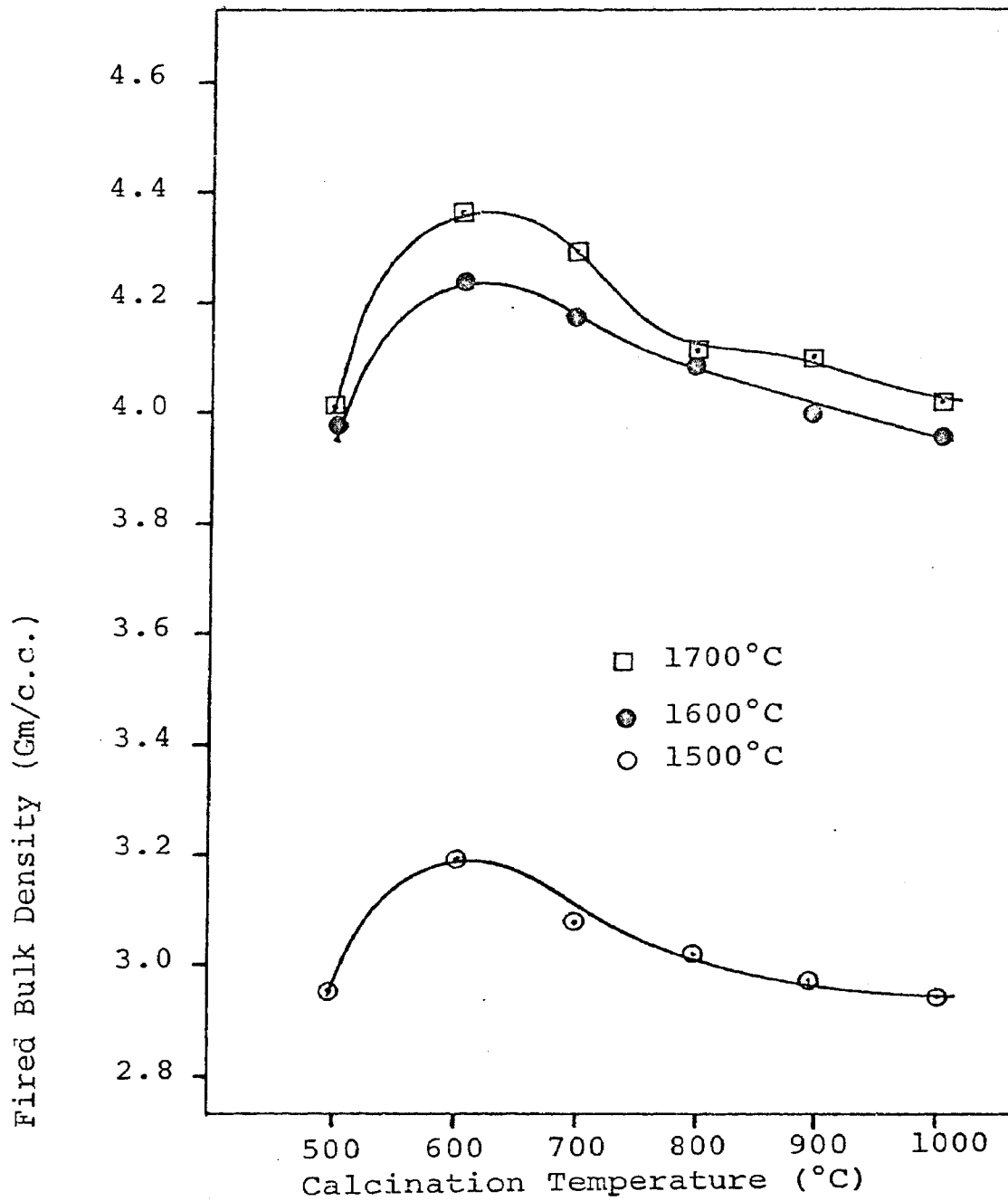
Figure 35.   Densities of Cr_2O_3 Pellets
             Fired in Nitrogen Atmosphere
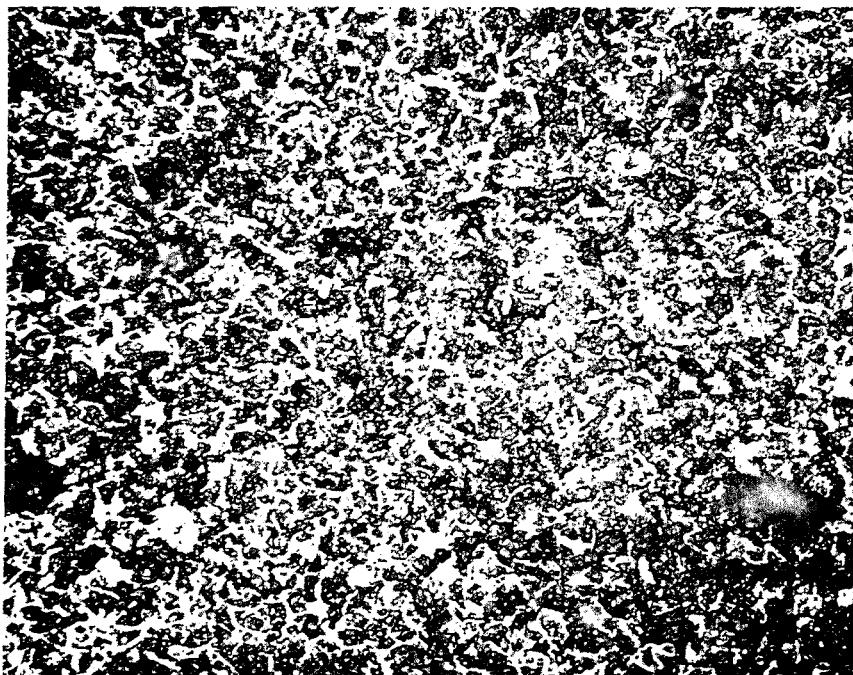
Figure 36. Photomicrograph of Sample Calcined at 500°C and Fired in Air at 1700°C   (250X)
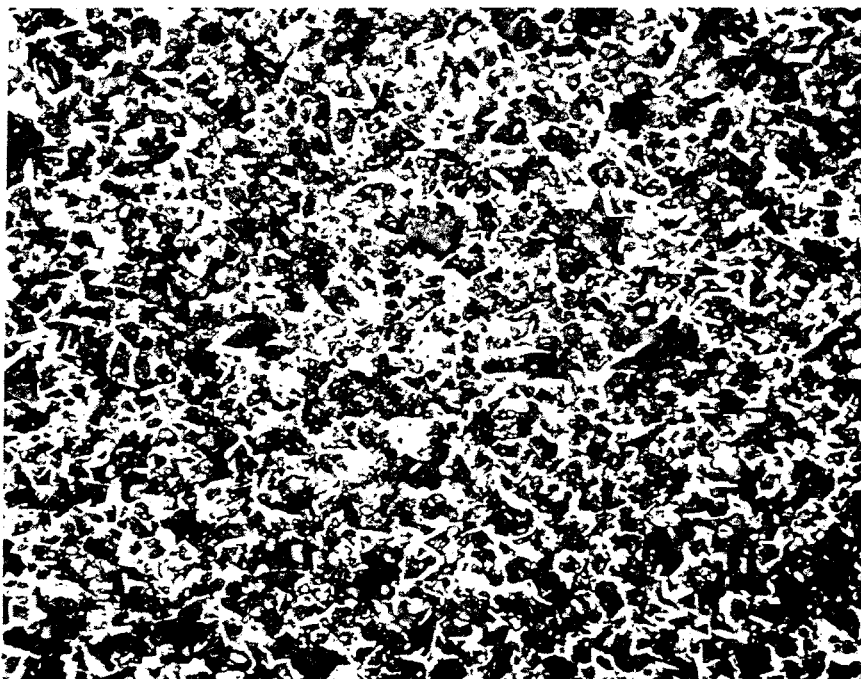
Figure 37. Photomicrograph of Sample Calcined at 700°C and Fired in Air at 1700°C   (250X)
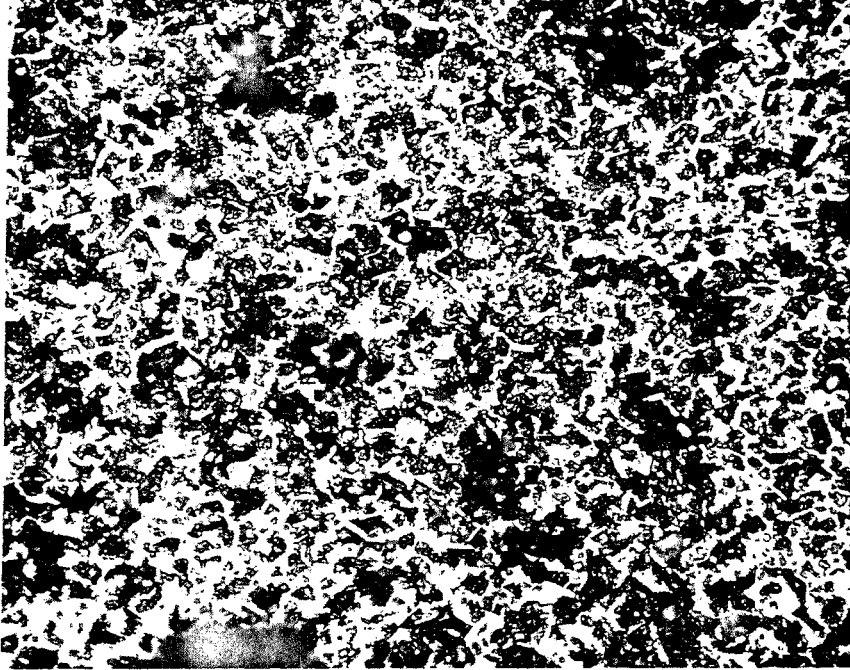
Figure 38. Photomicrograph of Sample Calcined at 900°C and Fired
in Air at 1700°C (250X)
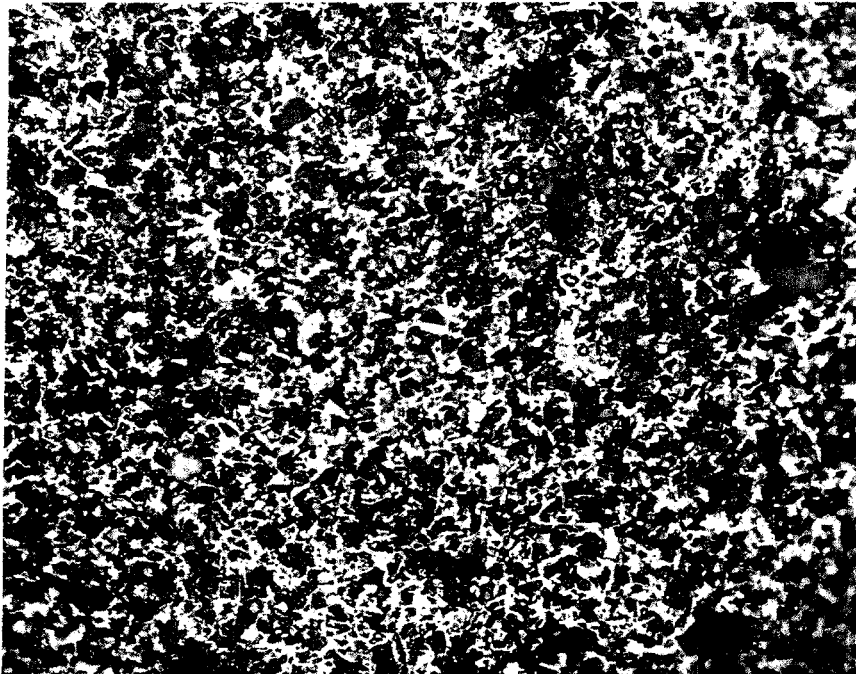
Figure 39. Photomicrograph of Sample Calcined at 500°C and Fired
in Oxygen at 1700°C (250X)
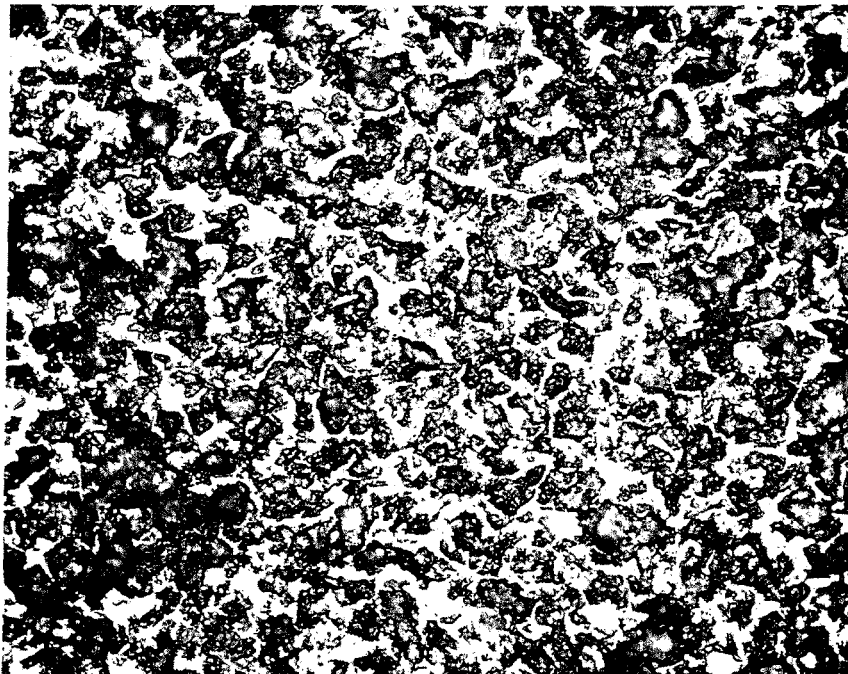
Figure 40.   Photomicrograph of Sample Calcined at 700°C and Fired
in Oxygen at 1700°C   (250X)
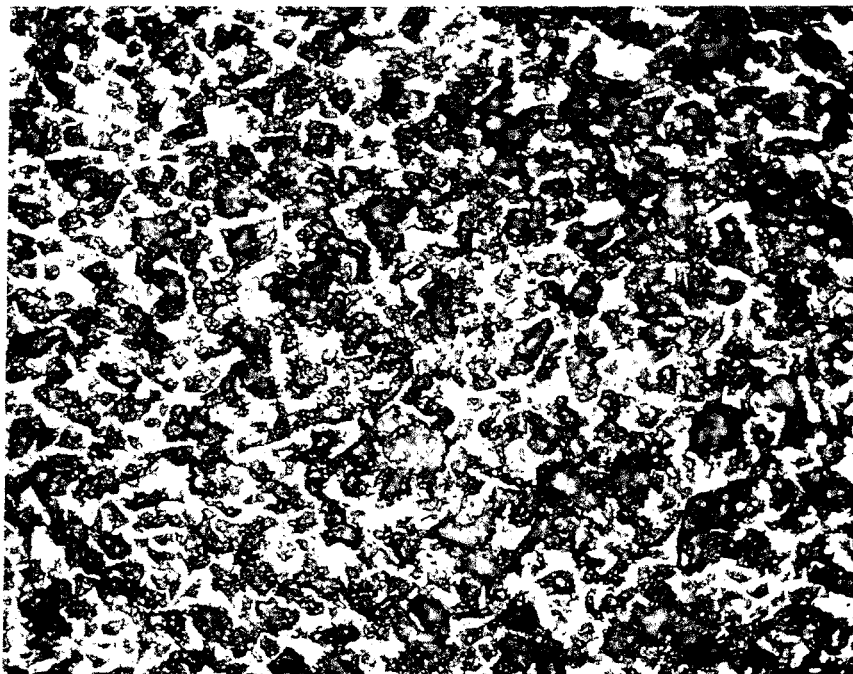
Figure 41.   Photomicrograph of Sample Calcined at 900°C and Fired
in Oxygen at 1700°C   (250X)
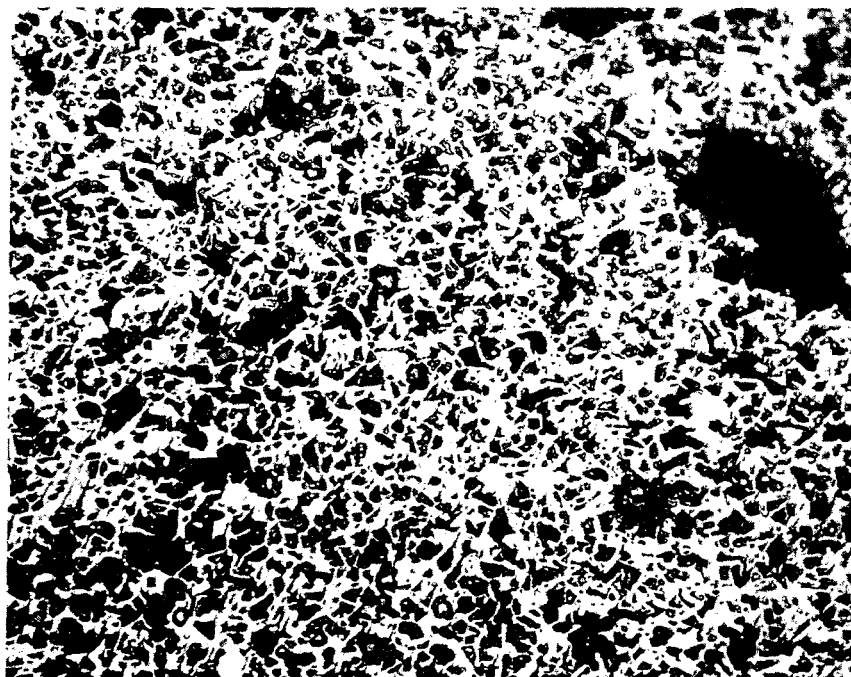
Figure 42. Photomicrograph of Sample Calcined at 500°C and Fired in Nitrogen at 1700°C (250X)
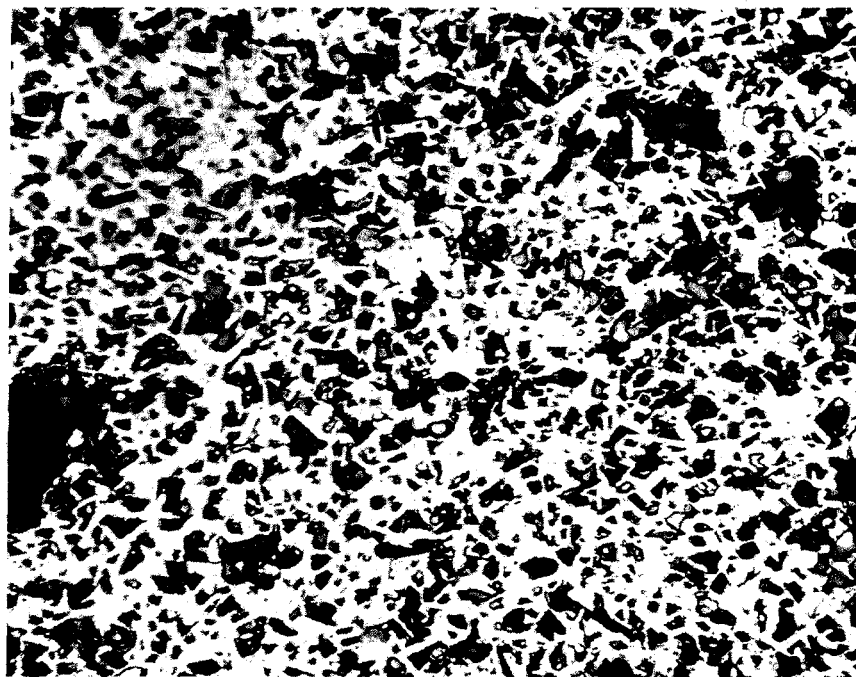
Figure 43. Photomicrograph of Sample Calcined at 700°C and Fired in Nitrogen at 1700°C (250X)
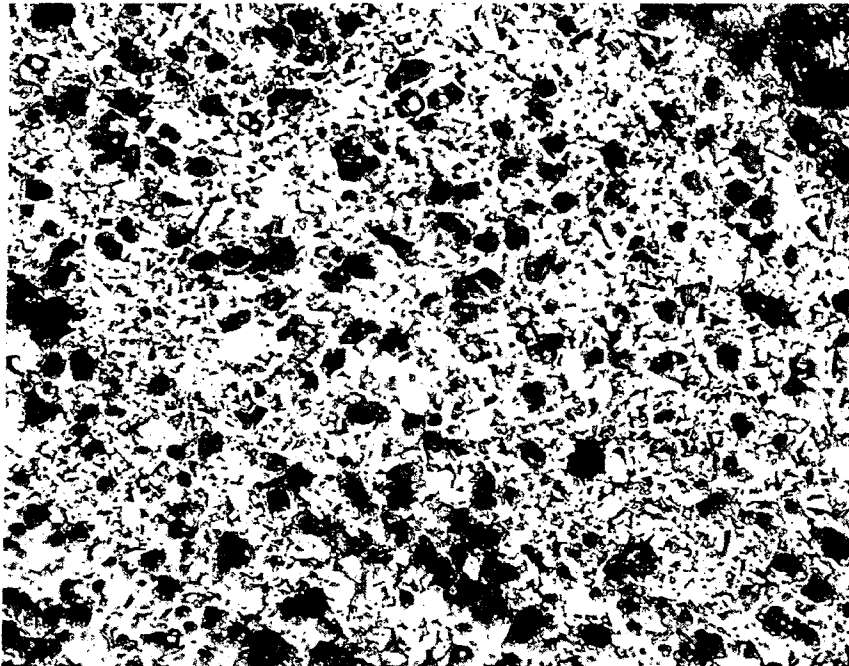
Figure 44. Photomicrograph of Sample Calcined at 900°C and Fired
in Nitrogen at 1700°C (250X)

V.   DISCUSSION OF RESULTS

A.   X-ray Diffraction Studies

X-ray diffraction analysis of the commercial $Cr(OH)_3$ gel showed that this material was amorphous. This is understandable as the commercial synthesis of $Cr(OH)_3$ involves the precipitation of the hydroxide from an ammonia solution and the formation of a gelatinous residue. Attempts to crystallize this gel by prolonged heating at low temperatures failed. The X-ray patterns obtained from the hydroxide samples heated to temperatures above 420°C showed peaks only for Cr_2O_3. The existence of an intermediate phase, $CrO(OH)$, has been confirmed by Laubengayer and McCune (26), but no evidence of this compound was observed under the present conditions of treatment.

The X-ray line broadening studies on the Cr_2O_3 powders produced by calcination yielded rates of crystallite growth at temperatures selected in the range of 700 to 1000°C, the data being shown in Figure 7. These growth rates are listed in Table 4.

Table 4.

Temperature	Crystallite Growth Rate
700°C	3.1 A°/hour
800°C	8.7 A°/hour
900°C	17.8 A°/hour
1000°C	39.0 A°/hour

It can be seen that the rate of crystallite growth increases substantially with temperature. Spurious results were obtained for samples heated below 700°C. This may be explained through one of the assumptions postulated for the application of this analytical method, viz., that each particle which diffracts the X-ray beam is a one-component crystal. In the particular case under study, if a particle were only partially decomposed, erroneous X-ray measurements could be expected due to $Cr(OH)_3$-Cr_2O_3 interfaces. This would particularly hold true for this system in which the $Cr(OH)_3$ is noncrystalline.

An energy of activation was calculated from the Arrhenius plot of logarithm of crystallite growth rate versus the reciprocal of absolute temperature. Data appear in Figure 8. A least square analysis of the growth rate data yielded an activation energy of 20±0.7 kilocalories per mole. This value lies at the low end of the range of energies usually reported for crystallite growth, viz., 20 to 50 kilocalories per mole. Fisher (29) has reported activation energies of 40, 49 and 64 kilocalories per mole for CaO crystallite growth processes for various crystallite sizes. Bicks and Friedman (30) present growth rates for MgO crystallites derived from the carbonate. An activation energy of 14 kilocalories per mole was calculated from these data. It appears therefore, that the various oxides exhibit widely varying activation energies for the crystallite growth process.

The crystallite growth process is thought to be similar to the grain growth process described in Kingery (31). Once nucleation, or primary recrystallization, has occurred resulting in a new crystal structure, an overall increase in grain size proceeds with little change in the grain size distribution. The driving force for the growth process is the difference in energy between the fine-grained material and the larger grain size material. The atomistic process necessary for grain growth is the jumping of an atom from a less energetically favorable site to a more energetically favorable site. Therefore, the temperature dependence is similar to that for diffusion, as represented by the equation for the diffusion coefficient, D:

$$D = D_o e(-Q/RT),$$

where Q is the activation energy of diffusion. The effect is that as the temperature is increased, the number of atoms present which have sufficient energy to overcome the activation energy barrier increases exponentially. Pertinence of this analysis is illustrated by the temperature dependence of the crystallite growth for Cr_2O_3 in this study.

B. Particle Size and Surface Area Analysis

The particle size data showed good correlation between the two methods of analysis. The parent gel had a median aggregate diameter of 3.9 microns, as determined from the Micromerograph data. The Micromerograph data yielded values for the calcined powders ranging from 3.3 to 5.2 microns,

while the Coulter Counter values ranged from 5.8 to 8.2 microns. For all samples, the Coulter Counter data resulted in the larger median diameters, by a ratio of approximately 1.5. An inherent characteristic of the equipment could explain this relation. The Micromerograph employs a de-agglomerator at the top of a fluid column to break up clusters prior to the separation of the size fractions. However, the only agitating action employed by the Coulter Counter is the mechanical stirring of the suspension. Thus, it appears that the Micromerograph is more capable of breaking up clusters, or agglomerated particles. From the particle size distribution curves seen in Appendix B and C, it is noted that typical sigmoid shape curves are obtained by both methods. The calcinations also produce particle size dis-tributions covering a narrow range of diameters. This is true for the size range over which the equipment operates although it is indicated from electron micrographs that there are particles smaller than the equipment used can measure.

Table 3 presents the correlation between crystallite size, particle size and surface area for selected calcines. From this table, a clearer relationship can be drawn between crystallite size and particle size. It is noted that a size ratio of approximately 100 exists between the crystallites and the aggregates of Cr_2O_3. The surface area values given

in this table compare favorably with the crystallite diameters. It can be seen that the crystallite sizes and surface areas change much more rapidly with temperature than do the aggregate diameters. Thus, it appears that the crystallite diameter is the contributing factor to the specific surface measured. In other words, the adsorption of gases on the calcined powders is dependent on the crystallite size rather than the aggregate size. This adsorptive capacity decreases very rapidly for samples of Cr_2O_3 calcined from the hydroxide at temperatures above 500°C. Thus, it is expected that the reactivity of the oxide would diminish sharply for samples calcined above about 500°C.

Another insight into the state of the powders can be gained by calculating the surface areas from the crystallite diameters assuming a spherical shape. The crystallites are not spherical, as will be observed in the electron micrographs, but it is common practice to assume a spherical surface area in calculational methods. Surface areas, calculated for selected calcined powders are compared to those measured by gaseous adsorptive capacities, in Table 5.

TABLE 5.

Surface Areas $(m^2/gm.)$

Sample	Measured	Calculated
700°C - 8 hours	15.4	23.6
800°C - 8 hours	4.10	15.8
900°C - 8 hours	1.03	9.8
1000°C - 8 hours	.82	7.2

The measurements indicate that the actual surface area decreases much more rapidly with increasing calcination temperature than could be detected from crystalline size measurements.

C. Decomposition Studies

These experiments explain many characteristics of the thermal decomposition of the $Cr(OH)_3$ gel. A marked difference is noted in the two weight loss versus temperature plots, Figures 10 and 12. Both curves result in two-step decomposition process. Under ambient heating conditions, these steps occur at about 100°C and 420°C. However, under a total pressure of approximately 100 microns, the second stage occurs at about 350°C. Vacuum decomposition also exhibits a less noticeable first stage, probably due to the room temperature dehydration effect under the reduced pressure. These two steps are commonly referred to in the literature as the dehydration stage and the oxide conversion stage.

The decomposition curves obtained under ambient con-
ditions and presented in Figure 11, show the effect of
increasing temperature on the degree of decomposition.
These curves indicate the amount of decomposition which
would be expected for a hydroxide sample under ambient
atmosphere heat treatments. It was observed that data taken
under these conditions were greatly influenced by sample
size, sample configuration and the container employed.

A more accurate picture of the decomposition process
can be obtained from plots obtained from decompositions
conducted under vacuum conditions. Data in Figures 13 and
15 indicate that the decomposition process is composed of
two distinct portions. The first portion, shown in Figure
13, relates to a rapid loss in weight, or high decomposition
rate. The second portion, seen in Figure 15, is associated
with a lower decomposition rate. These two portions, as
represented in the general decomposition curve in Figure 2,
are commonly described as the acceleratory region and the
decay region. It is quite common for no induction period
to be observed for empirical plots, since this region is
considered to relate to the heating up process and so is
rate dependent.

An activation energy for decomposition was calculated
by plotting the logarithm of the decomposition rates in
Figure 13 versus the reciprocal of the absolute temperature.

A least squares analysis of these data yielded an activation energy of 25±0.8 kilocalories per mole. This value compares favorably with the activation energies found for the decomposition of other hydroxides, which range from 10 to 70 kilocalories per mole. Gregg and Razouk (32) reported activation energies for the thermal decomposition under vacuum of precipitated $Mg(OH)_2$ ranging from 12.4 to 27.4 kilocalories per mole, depending on the preparation of the various precipitates. As noted in the literature survey, Eyraud and Goton (13) found an activation energy of decomposition of 31 kilocalories per mole for aluminum hydroxide.

The theoretical mechanism governing the decomposition of $Cr(OH)_3$ is assumed to be an interface model as evidenced by the long linear portion of the rate plots in Figure 13. This interface model predicts that the rate is proportional to the particle surface area or to the number of reaction sites per area. The reaction interface can be visualized as a spherical layer which progressively moves inward from the surface of the particle. It appears that the reaction proceeds unhindered during the acceleratory region, but the impingement of the reaction zones of neighboring particles produces a barrier to the removal of the reaction products as evidenced by the decay region. It is also noted that the acceleratory region observed for the $Cr(OH)_3$

gel is of shorter duration than for crystals of $Mg(OH)_2$ and other hydroxides indicating that this impingement action takes place sooner for the $Cr(OH)_3$ gel. This is presumably so because of the fine size of the gel particles.

The fraction decomposed, α, and the elapsed time for these decompositions were plotted according to the equations formulated by Mampel (11). Plots of $(1-\alpha)^{1/3}$ versus time and log α versus log time were developed, but did not appear to fit the data very accurately. Plotting log $(1-\alpha)$ versus time produced linear relationships for the major portion of the heating period. It is generally considered satisfactory if a relationship holds true for greater than sixty per cent of the reaction time. Linearity of the log $(1-\alpha)$ versus time relationship, as used by Gordon and Kingery (15), is considered to be a check for first-order reaction kinetics. Mampel employs this relationship to describe the decay portion of a decomposition curve where a unimolecular reaction is believed to occur. He states that for very fine powders nearly the entire decomposition follows the unimolecular law. The reason for this is that for large particles, the surface becomes covered with nuclei, while for small ones, a particle is consumed by the reaction spreading from a single nucleus. It is quite natural for the data to fit relationships describing both first-order reaction kinetics and a

unimolecular law. In the earlier literature, the term
unimolecular was used to denote a reaction of the first
order. However, in actuality, reaction order applies to
the experimental equation and molecularity applies to the
theoretical mechanism.

D. Photographic Studies of Powders

The light microscope and the electron microscope pro-
vided complementary advantages for the observation of the
calcined powders. The photomicrographs illustrate the
aggregated nature of the powders. Measuring a typical
aggregate on a photograph, Figure 22, yields a diameter of
about 0.5 centimeters. At a magnification of 500 times,
this results in an aggregate diameter of 10 microns. This
value compares favorably with the median particle sizes
listed in Table 3. Judging from the photograph, there
appear to be many aggregates of smaller sizes. The in-
crease in aggregate size with calcining temperature is
quite apparent from comparison of the photomicrographs of
the samples calcined for both two and eight hour periods.
This indicates that there is definitely some initial sin-
tering at even low temperatures.

The electron micrographs serve for assessment of the
degree of crystallinity and estimation of the size of the
crystallites in the calcined powders. The samples cal-
cined for two hour periods exhibit small, almost undetect-
able, crystallites, but only at the higher calcination

temperatures of 800 and 900°C. However, small crystallites
are observable in the micrograph of the sample calcined
for eight hours at 500°C and considerable crystallite
growth is evidenced at the 600, 700, 800 and 900°C levels
after eight hour periods. These electron micrographs
should be compared with the micrograph of the commercial
gel in Figure 35, which revealed no evidence of crystal
structure. However, micrographs of the samples calcined
for eight hours exhibit definite hexagonal platelets,
many of which rest on their basal plane. It is assumed
that the acicular looking areas are actually platelets
on edge. Measurement of a typical platelet on the photo-
graph of the sample calcined eight hours at 900°C yields
a diameter of about 0.1 centimeter. For a magnification
of 10,000 times, this corresponds to a crystallite dia-
meter of 1000 Angstrom units, comparing favorably with
the value of 970 Angstrom units as determined for the
same sample from Figure 7. The electron diffraction
pattern, seen in Figure 36, was obtained from one of the
larger crystallites of the sample calcined eight hours
at 900°C, and is the diffraction pattern expected from
the basal plane of a hexagonal crystal. It is apparent
from these micrographs that the aggregates are composed
of many small crystallites with a myriad of orientations.

E.   Sintering Studies

The sinterability of the calcined Cr_2O_3 powders can be assessed from the density measurements of the sintered pellets and the photomicrographs of these pellets. A calcination period of two hours was chosen for the production of the powders since it was evident that the decomposition was nearly complete at this stage, and yet the powders still exhibit large surface areas. Density measurements indicate that a calcination temperature of 500°C is optimum. This calcination temperature resulted in the highest sintered densities at all subsequent firing temperatures and under all three sintering atmospheres. As would be expected, the sintered densities increased with increased firing temperature. As had been noticed before in the case of Cr_2O_3, it was difficult to sinter the material to a density approaching the theoretical density of 5.21 grams per cubic centimeter. The closest approach to this value was observed for pellets fired under a nitrogen atmosphere, resulting in a maximum density of 4.35 grams per cubic centimeter. Firing in an oxygen atmosphere resulted in the lowest bulk densities for the Cr_2O_3 pellets. This is probably due to the enhanced evaporation of CrO_3 arising from the oxygen atmosphere. Margrave and co-workers (33) have found that at high temperatures, Cr_2O_3 decomposes to form gaseous CrO_3 under oxidizing conditions.

Thus, the volatilization of CrO_3 would act to compete against the diffusion processes necessary for successful sintering, since the evaporation-condensation mode of material transport does not result in an overall shrinkage during sintering. The photomicrographs also illustrate the effectiveness of a nitrogen atmosphere upon sintering of Cr_2O_3. The pellets shown in Figure 42 through 44 exhibit more necking and closer bonding than pellets sintered in air or oxygen.

VI.   SUMMARY AND CONCLUSIONS

The results of this study are summarized in the following statements:

1.   The chromium hydroxide gel used in this study undergoes a two-step decomposition process. The first step is a dehydration process while the second step is the oxide conversion step which occurs at about 420°C in ambient atmospheres.   The hydroxide is converted to alpha Cr_2O_3 without the formation of any intermediate phases or other oxides of chromium.

2.   The decomposition curves exhibit an acceleratory portion and a decay portion.   The curves for decompositions conducted in air were markedly affected by the sample size and the packing conditions.   An activation energy of 25 ±0.8 kilocalories per mole was calculated from the decomposition process rates under vacuum conditions. The major portion of the decomposition process followed a unimolecular, first-order reaction kinetics relationship.   An interface model was suggested as the mechanism responsible for the decomposition reaction.

3. Crystallites of Cr_2O_3 exhibit an increased growth rate with increased temperatures over the range of 700 to 1000°C. An activation energy of 20 ±.07 kilocalories per mole was determined for this process. It was suggested that this crystallite growth process is controlled by solid state diffusion and is similar to grain growth in polycrystalline ceramics.

4. The nature of the Cr_2O_3 powders, as revealed by electron micrographs, consists of loosely-packed arrays of hexagonal platelets. The surface area of these powders exhibited a maximum of 57.9 square meters per gram at a calcination temperature of 500°C.

5. The optimum calcination temperature was found to be approximately 500°C. The maximum sintered densities were obtained by firing in a nitrogen atmosphere, while the lowest densities were obtained by firing in an oxygen atmosphere.

VII. SUGGESTIONS FOR FUTURE WORK

Several observations have been made during the course of this research which are pertinent to future work in the area of active Cr_2O_3 powders. In decomposition studies of this nature, it is important to use a parent material of a known chemical composition and particle size. In the specific case of a hydroxide, it is important that the water of hydration content be known very precisely. It is also very important to employ a crystalline material which can be identified by X-ray techniques as a definite mineralogical compound.

From the standpoint of active powders, it should prove beneficial to study the production of active Cr_2O_3 from other chromium compounds such as the carbonate, oxalate and others. Properties of these calcined powders, such as particle size and surface area, could then be compared to those of the calcined hydroxide material.

The effect of sintering additives to Cr_2O_3 should be studied in order to determine the optimum sintering conditions for Cr_2O_3. Various types of additives, especially reducing agents or oxides which form solid solutions with Cr_2O_3, could be selected.

APPENDIX

APPENDIX A.

An example data sheet for the Coulter Counter measurements is shown on the following page. The data of a two-hour calcination at 800°C is presented. Following this sheet is an explanation of the procedure for handling such data.

COULTER ELECTRONICS INDUSTRIAL DIVISION — 2001 Mannheim Road, Franklin Park, Illinois 60131
INDUSTRIAL MODEL B
COULTER COUNTER DATA AND WEIGHT CONVERSION
SINGLE THRESHOLD

Sample: 800-2 Source: ___ Electrolyte: 1% NaCl Date: 4/5

Aperture Diameter: 50 μ Manometer Volume: 50 μl Coinc. Factor p = 3.125 Calib. Factor k = 3.0 Dispersant: ___ Oper.: T.A.C.

Aperture Resistance: 11,000 Ω Gain Control: 100 Matching Switch: 64H Calibration Data: ___

t_L	!	Λ	n' (raw counts)				$\bar{n}'$	$p\left(\frac{n''}{1000}\right)^2$ ✓	$n = \bar{n}' + n''$	$V = k \cdot t_L \cdot I \cdot A$	$d_L = 1.241\sqrt[3]{V_L}$
5	2	32	76	56			66	—	66	960	12.2
	2	16	163	145			154	1	155	480	9.71
	2	8	540	840			695	2	697	240	7.71
	2	4	1670	1940			1805	10	1915	120	6.12
	2	2	3350	3260			3305	34	3339	60	4.86
	2	1	5470	5580			5525	95	5620	30	3.86
	2	1/2	8730	8560			8645	233	8878	15	3.06
	2	1/4	12,230	12,270			12,250	469	12,719	7.5	2.42
	2	1/8	17,390	16,850			17,120	915	18,035	3.75	1.92
1	1/8		19,450	19,720			19,585	1198	20,783	1.87	1.42
1/2	1/8		21,140	22,000			21,570	1453	23,023	.93	1.21
1/4	1/8		24,580	25,770			25,175	1981	27,156	.46	.96

Δn	$\bar{V}$	(Δn)$\bar{V}$	Σ(Δn)$\bar{V}$	Wt. %
89	720	64,080	64,080	7.4
542	360	195,120	259,200	30.1
1118	180	204,240	460,440	53.5
1524	90	137,160	597,600	69.4
2281	45	102,645	700,245	81.4
3258	22.5	73,305	773,550	89.9
3841	11.2	43,091	816,641	94.9
5316	5.6	29,769	846,410	98.4
2749	2.8	7694	854,104	99.2
2240	1.4	3136	857,240	99.6
4133	.7	2893	860,133	100

For downward Σ, plot wt. % vs. lower "d" values; if upward Σ, use upper "d" values.

76

APPENDIX A.

Data Reduction for Coulter Counter

1. The spaces at the top of the sheet are filled in
    with the appropriate information. The value for
    the coincidence factor is obtained from the equation:

    $$\rho = 2.5 \left(\frac{D}{100}\right)^3 \left(\frac{500}{V}\right)$$

    where D = aperture diameter in microns, and

    V = manometer volume in microliters.

    The value for the calibration factor is derived under
    the calibration procedure. The values for aperture
    resistance, gain control and matching switch were
    obtained from those suggested by the Coulter Company,
    and were maintained constant for all measurements.

2. The first three columns contain the values used for
    the lower threshold setting, aperture current setting,
    and the amplification factor, respectively.

3. The columns under n' are used to record the raw data
    in number of counts which are averaged under the
    column headed $\bar{n}'$.

4. The next column gives the proper coincidence correction
    using the formula:

    $$n'' = \rho \left(\frac{\bar{n}'}{1000}\right)^2$$

5. The column headed n is obtained by adding the values under $\bar{n}'$ and n".

6. The column headed V is obtained by multiplying the values under k, t_L, I and A, and represents the particle volume in cubic microns.

7. The column headed d_L contains the values for particle diameter.

8. The column headed Δn is obtained by subtracting each pair of successive counts for the n values.

9. The next column shows the average of each pair of successive particle volumes.

10. The column headed (Δn)$\bar{V}$ is obtained by multiplying the values under the two previous columns.

11. The next column is obtained by cumulatively adding values from the column headed (Δn)$\bar{V}$.

12. The last column is obtained by assigning 100 per cent to the value in the (Δn)$\bar{V}$ and then calculating the per cent of each other value based on the 100 per cent value.

13. Weight or volume per cent greater than the stated size may be plotted versus particle diameter on semilog paper by plotting each value of particle diameter against the upper per cent value of the weight per cent column.

APPENDIX B.

Particle Size Distribution from Coulter Counter Data
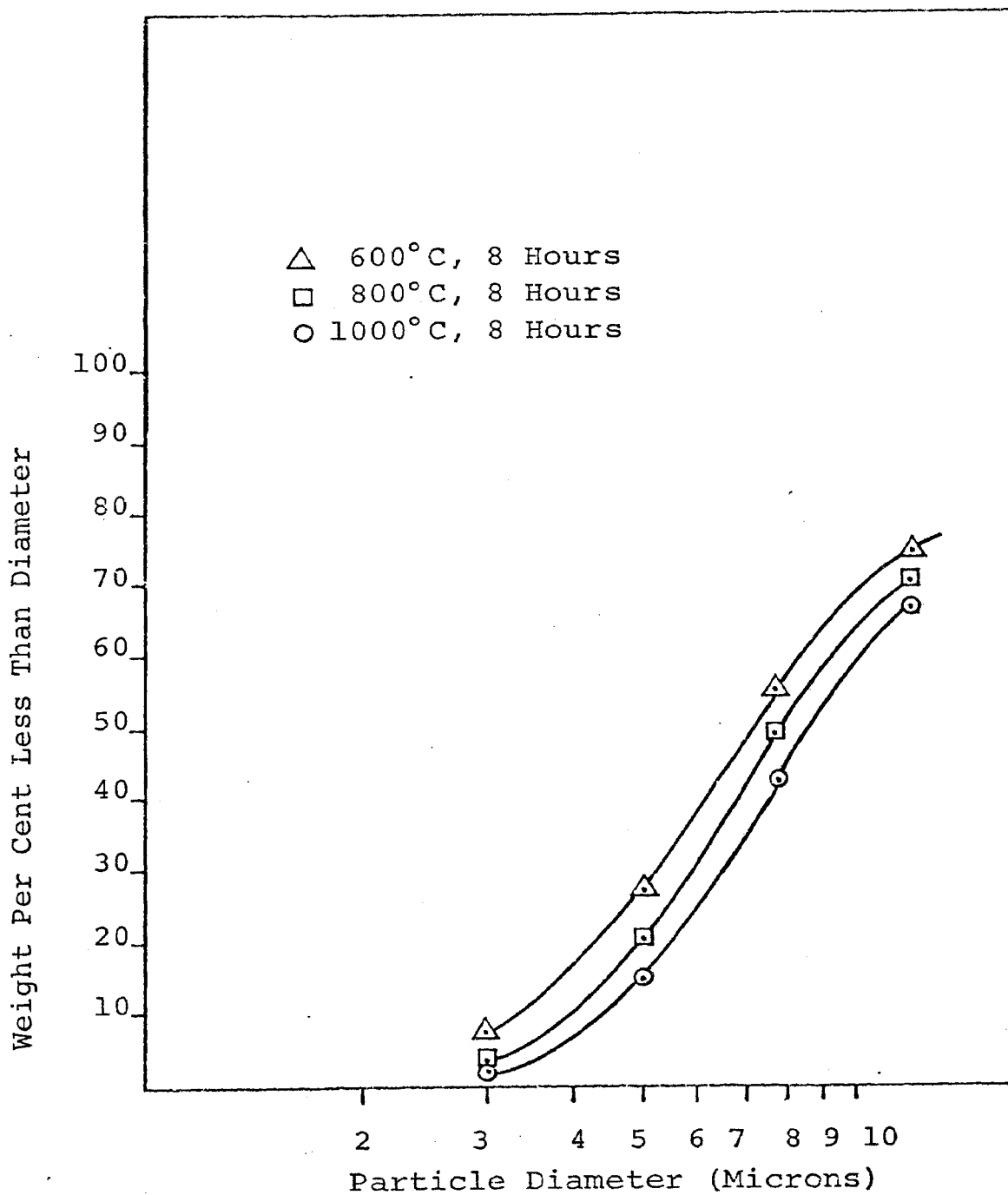
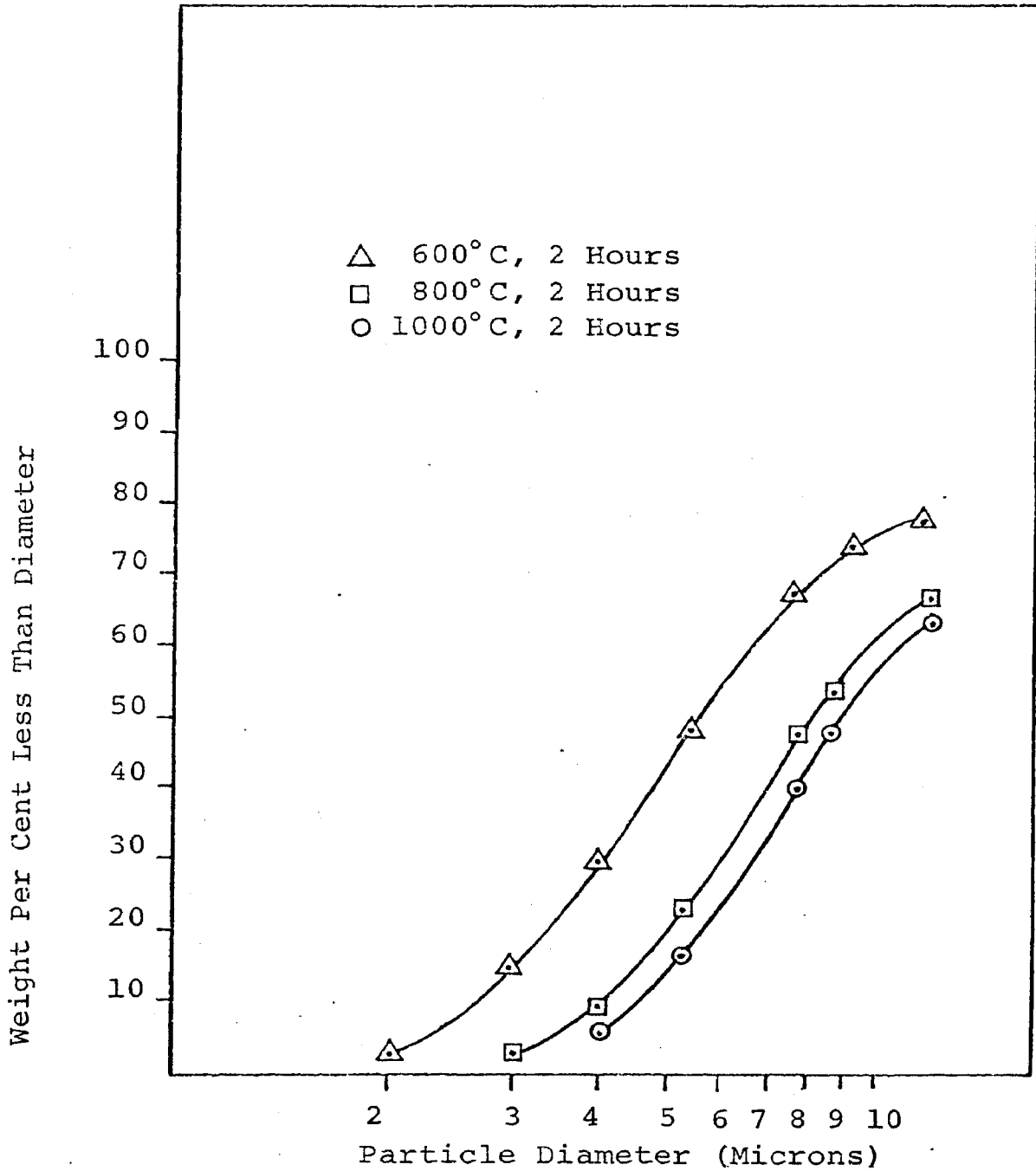Figure B-1. Coulter Counter Particle Size
Distribution for Selected
Calcines

Figure B-2.   Coulter Counter Particle Size
              Distribution for Selected
              Calcines
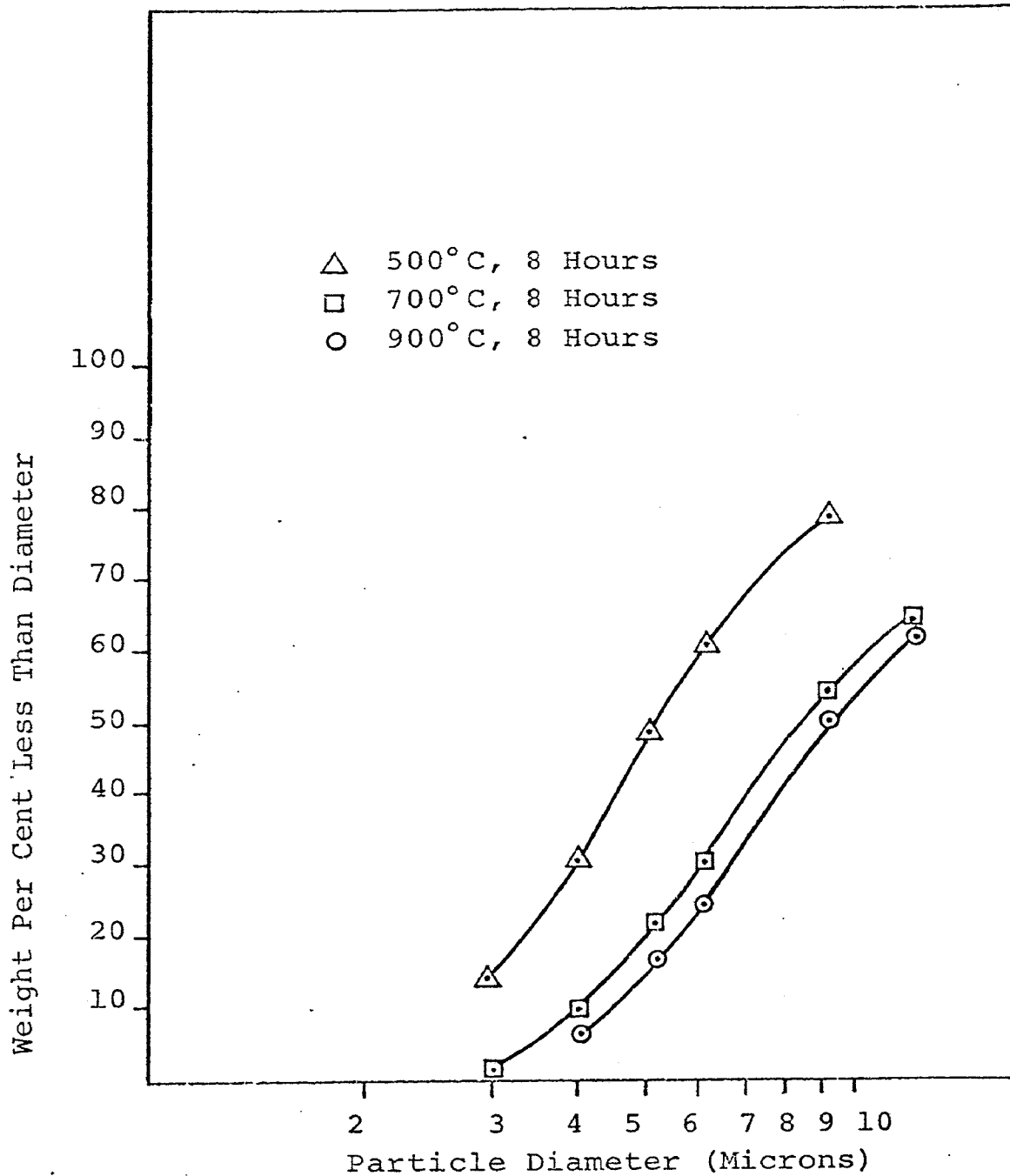
Figure B-3.   Coulter Counter Particle Size
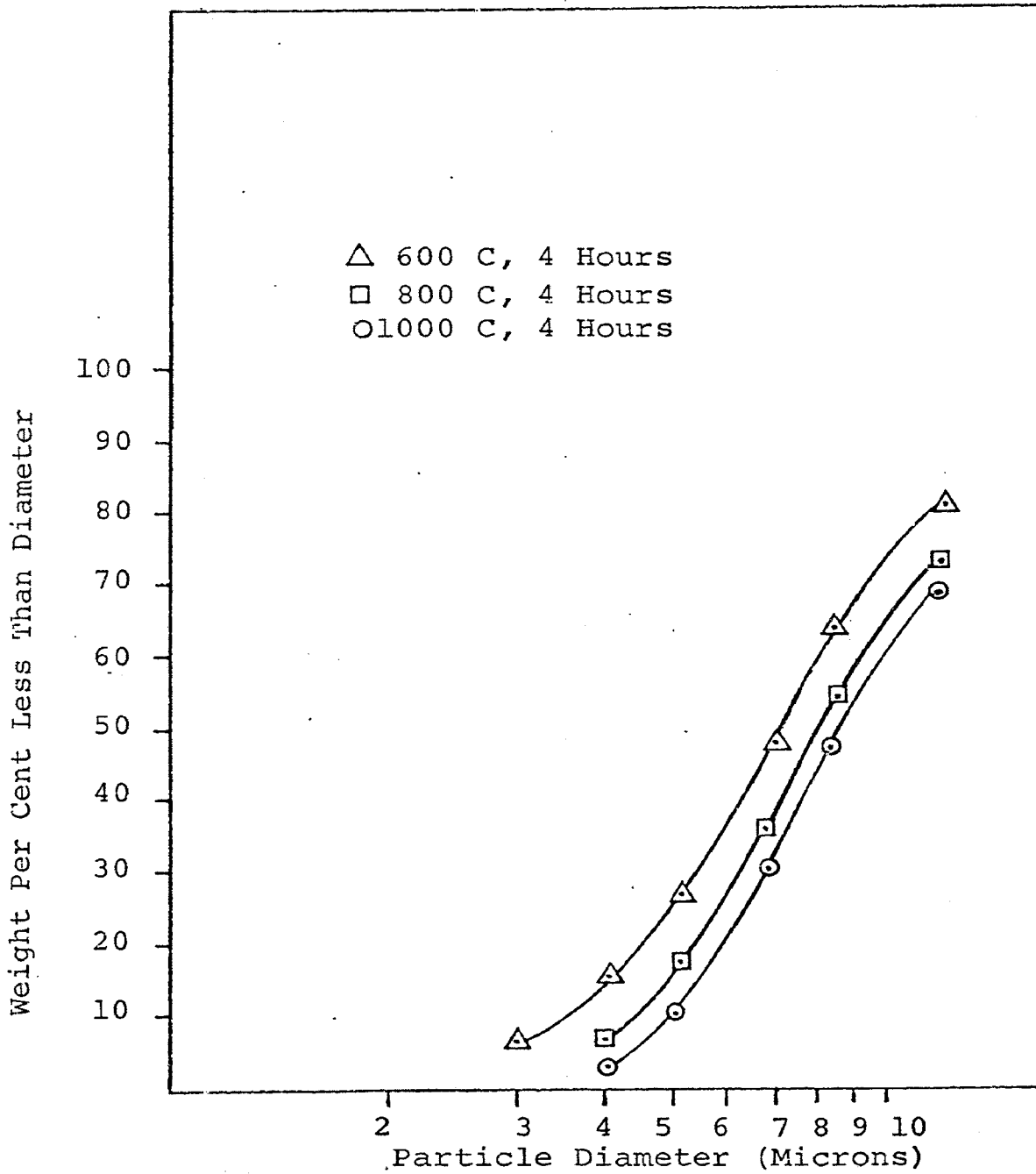   Distribution for Selected
              Calcines

Figure B-4.   Coulter Counter Particle Size
              Distribution for Selected Calcines

APPENDIX C.

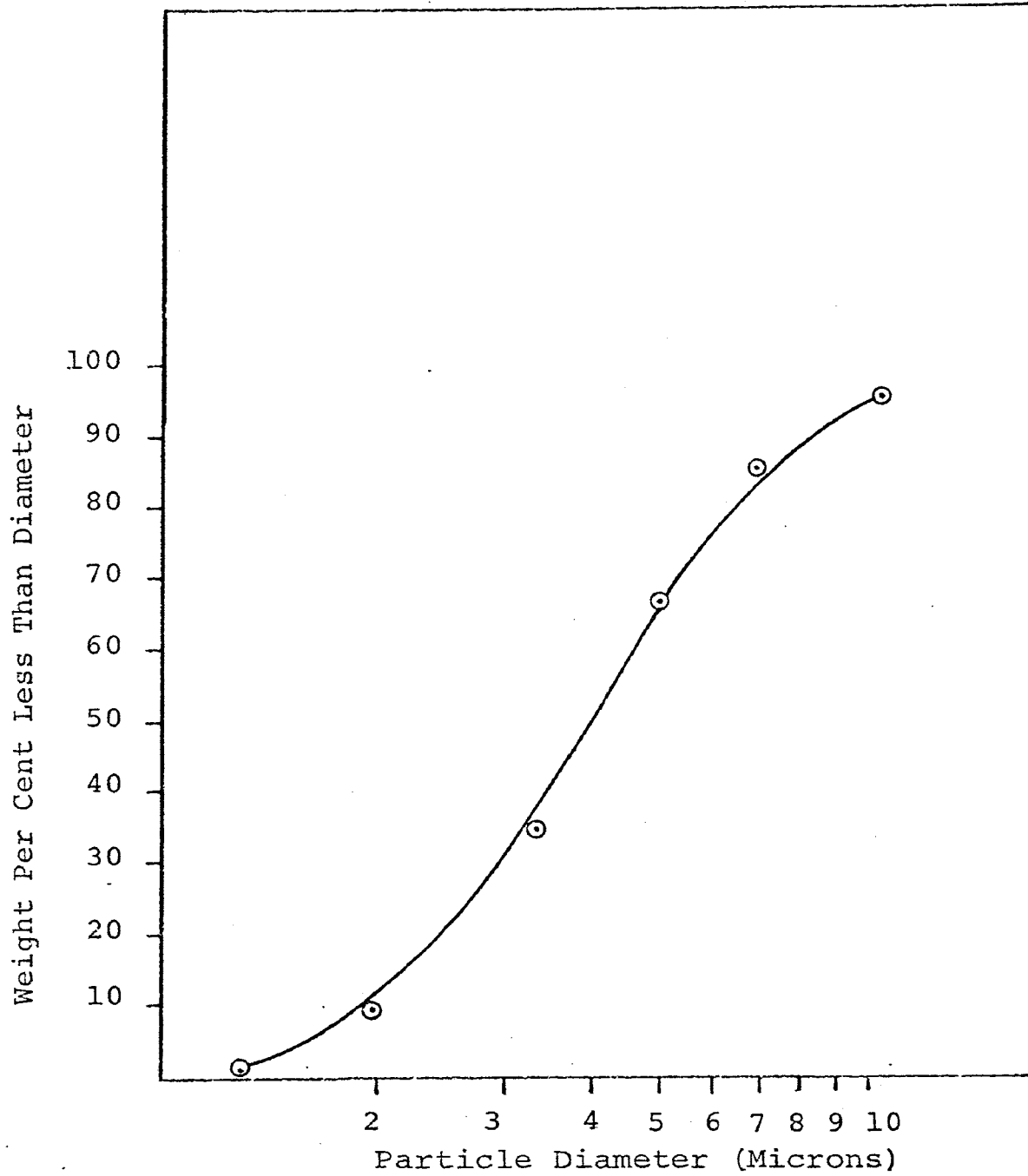
Particle Size Distributions from Micromerograph Data

Figure C-1.   Micromerograph Particle Size
Distribution for $Cr(OH)_3$ Gel

Figure C-2.   Micromerograph Particle Size
             Distribution for Selected
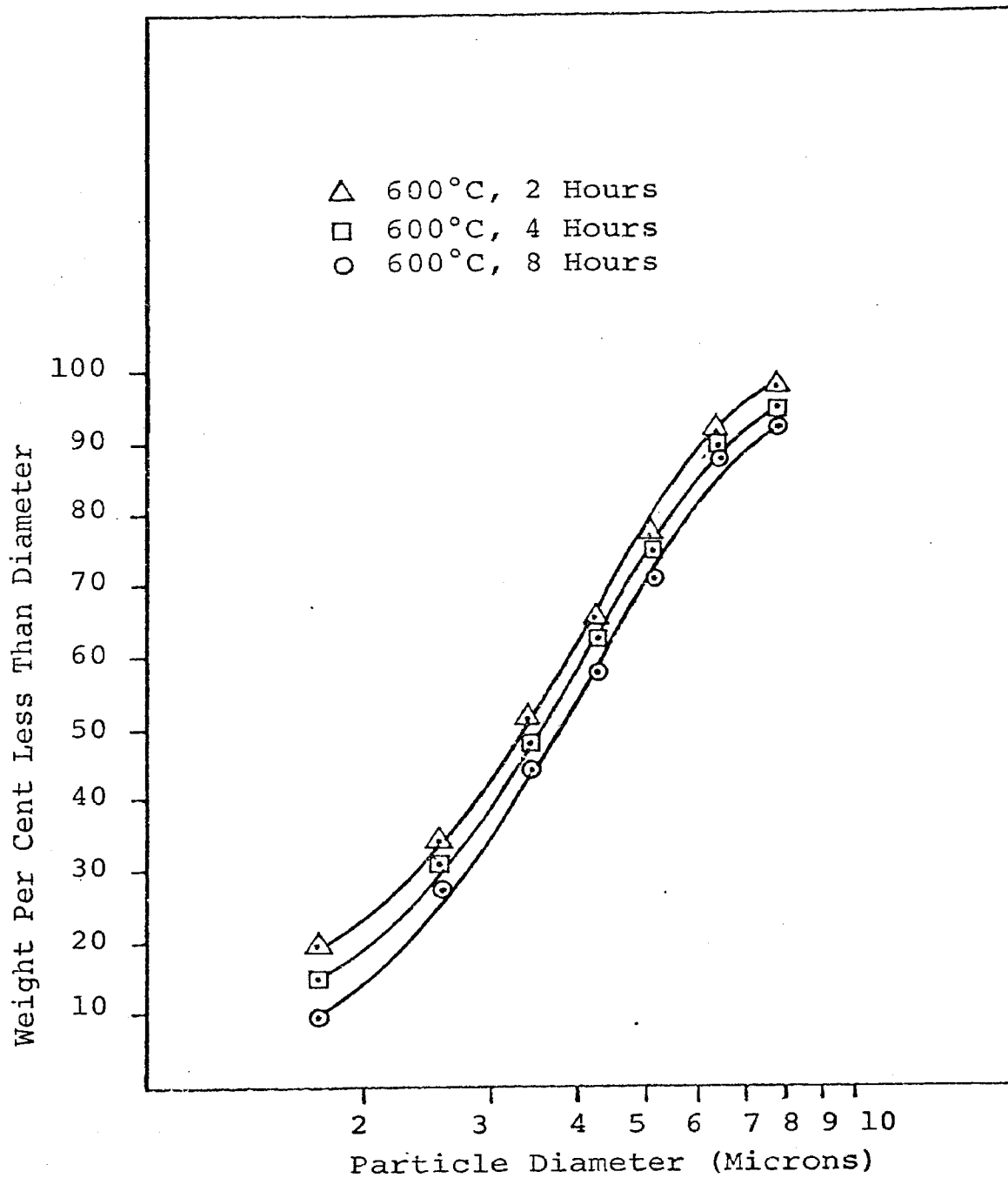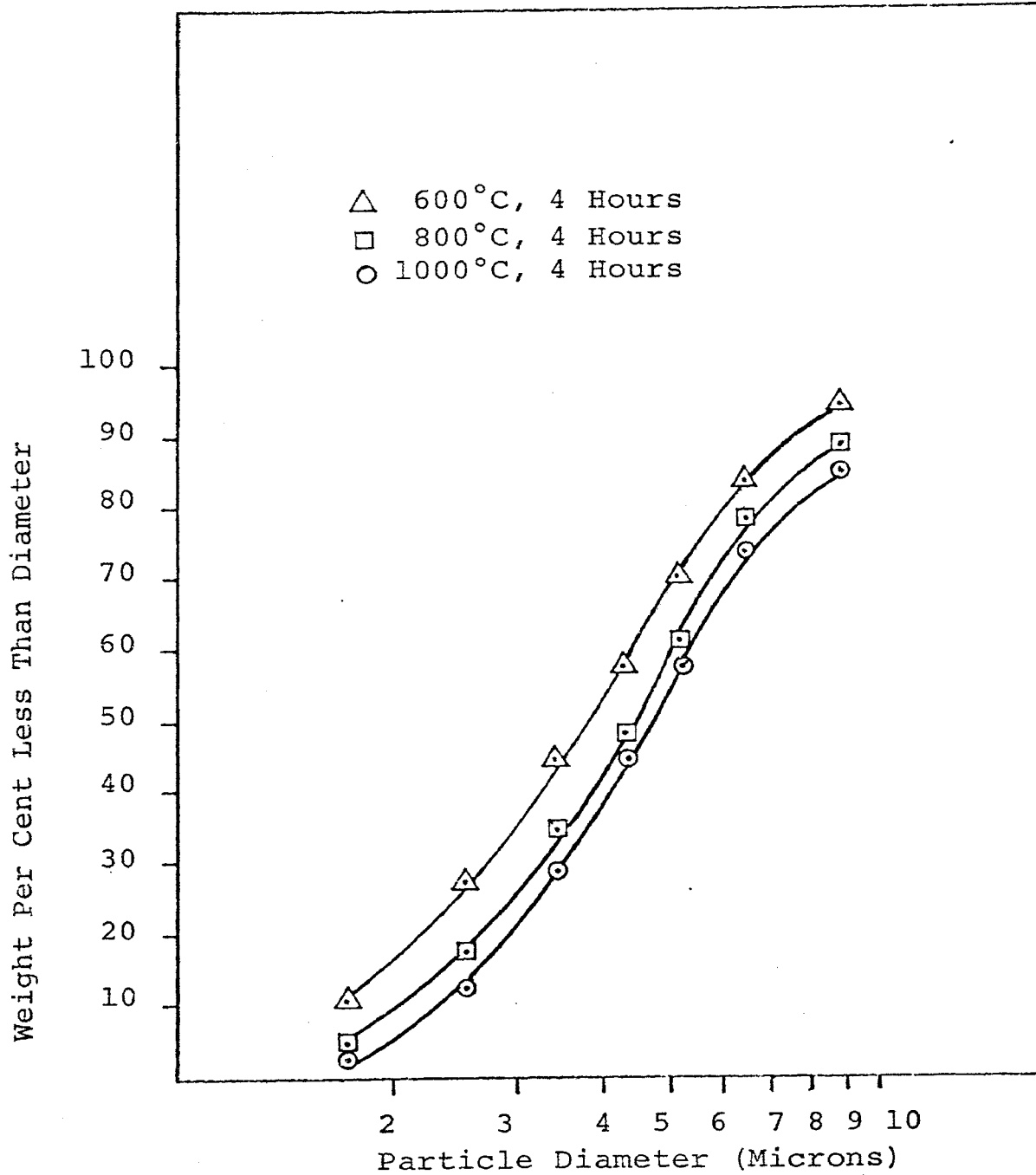   Calcines

Figure C-3.   Micromerograph Particle Size
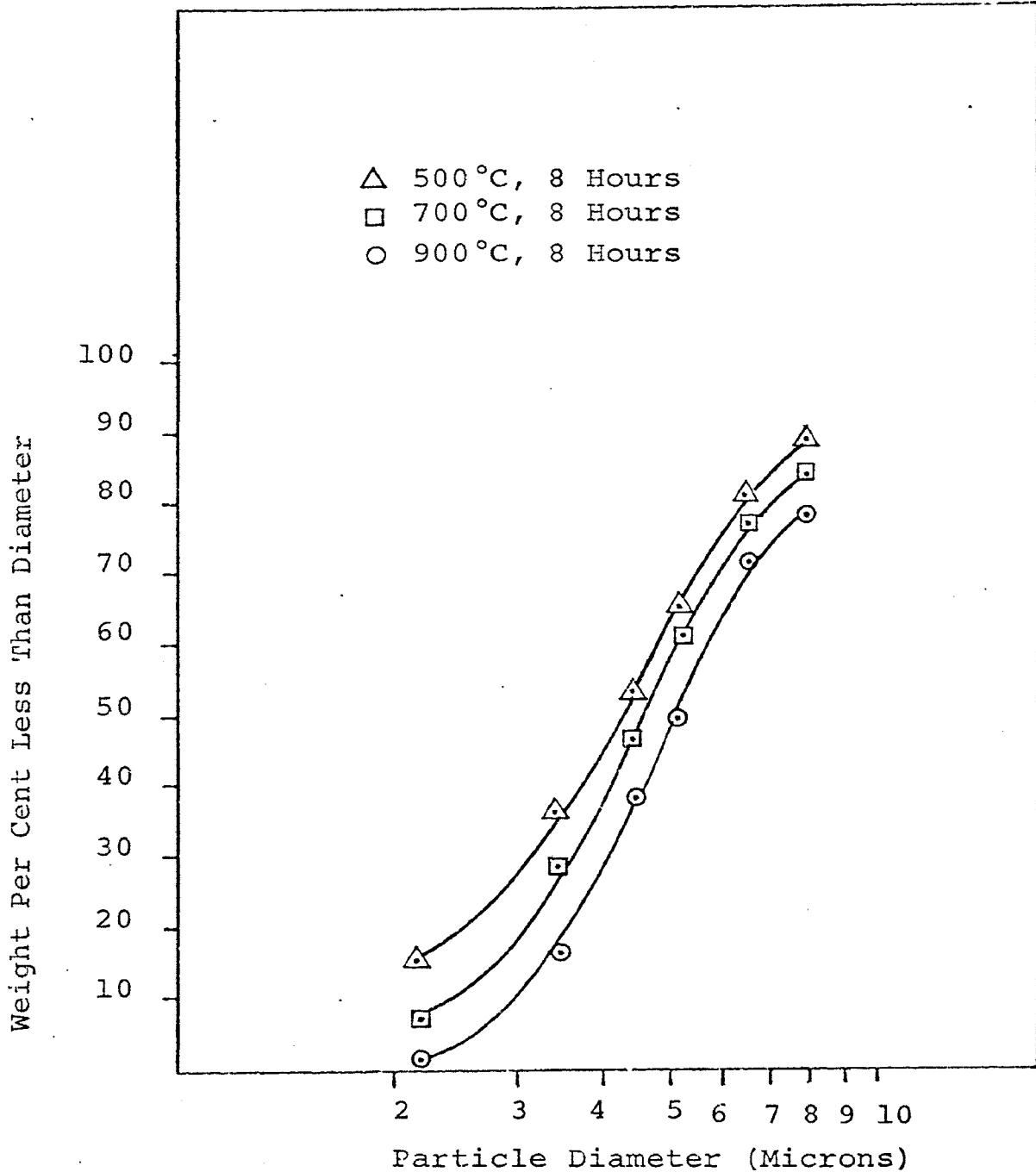Distribution for Selected
Calcines

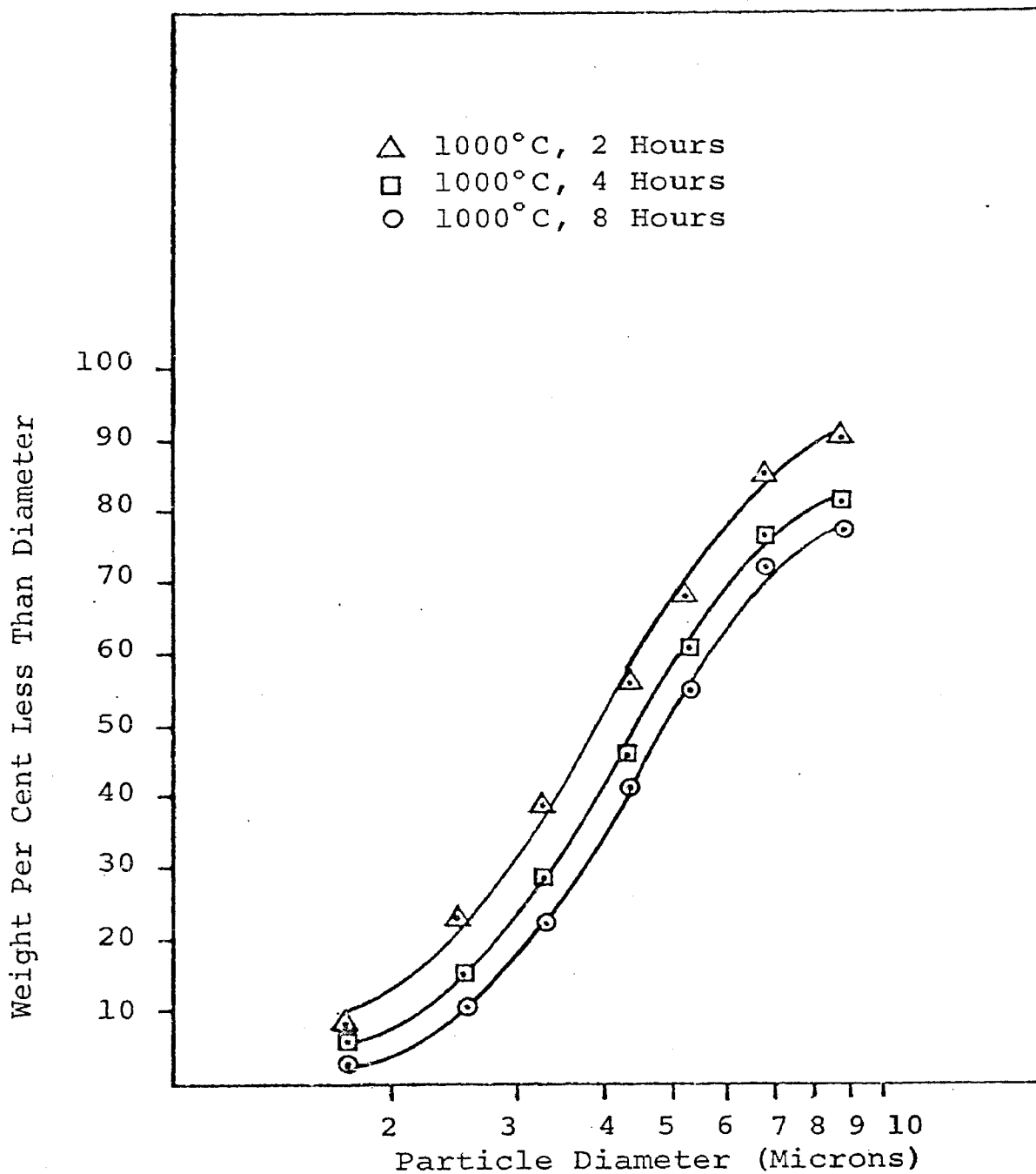Figure C-4. Micromerograph Particle Size Distribution for Selected Calcines

Figure C-5.   Micromerograph Particle Size
              Distribution for Selected Calcines

APPENDIX D.

X-ray and DTA Patterns for Commercial Gel
and Synthesized $Cr(OH)_3$

APPENDIX D.

The synthesis of a crystalline $Cr(OH)_3$ material
was conducted following the procedure outlined by Roy
and Shafer (27). Chromium hydroxide was formed by
reacting $CrCl_3$ and NH_4OH with an excess of ammonia.
The precipitated hydroxide gel was centrifuged,
decanted and sealed in a rubber balloon. This balloon
was pressurized in an isostatic cavity containing
glycerine as a pressure-transmitting fluid at a pressure
of 12,000 pounds per square inch for 72 hours. The
material was then removed and allowed to air-dry. X-ray
diffraction and differential thermal analyses were run
on this material and are compared to the analyses of the
commercial hydroxide gel, as shown in Figures (D-1 through
D-4).
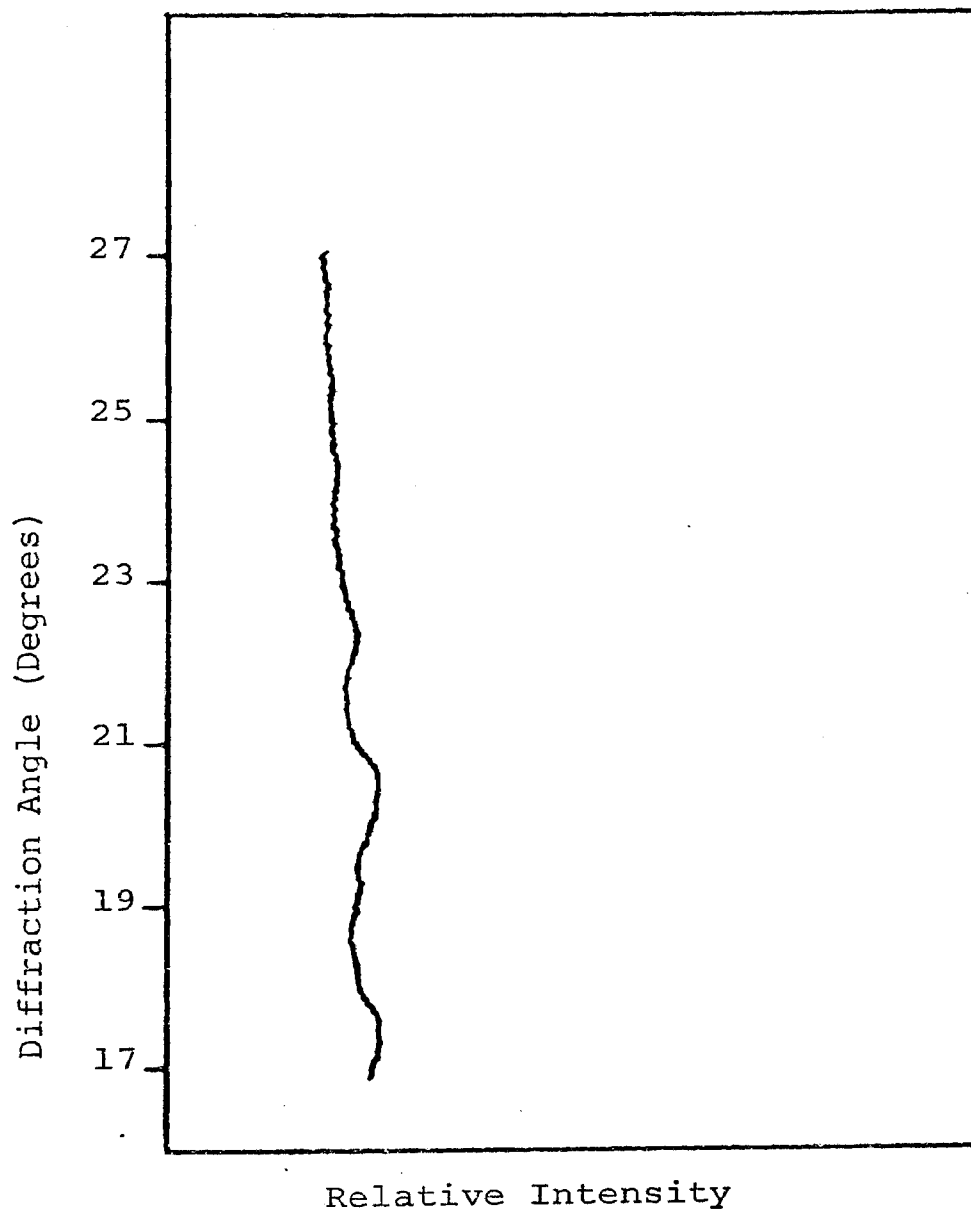
Figure D-1.   X-ray Diffraction Pattern
for $Cr(OH)_3$ Gel
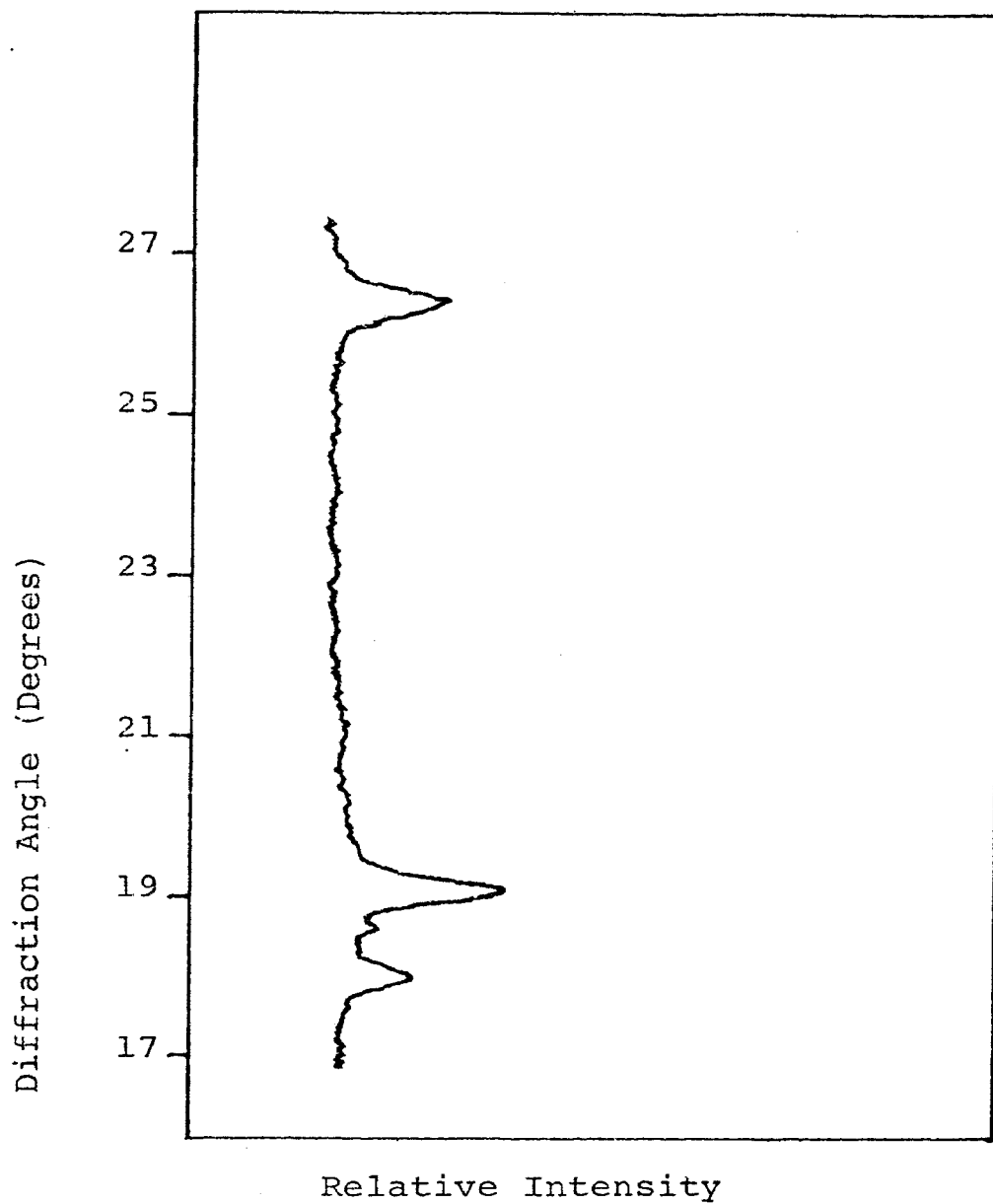
Figure D-2. X-ray Diffraction Pattern
for Synthesized Cr(OH)$_3$
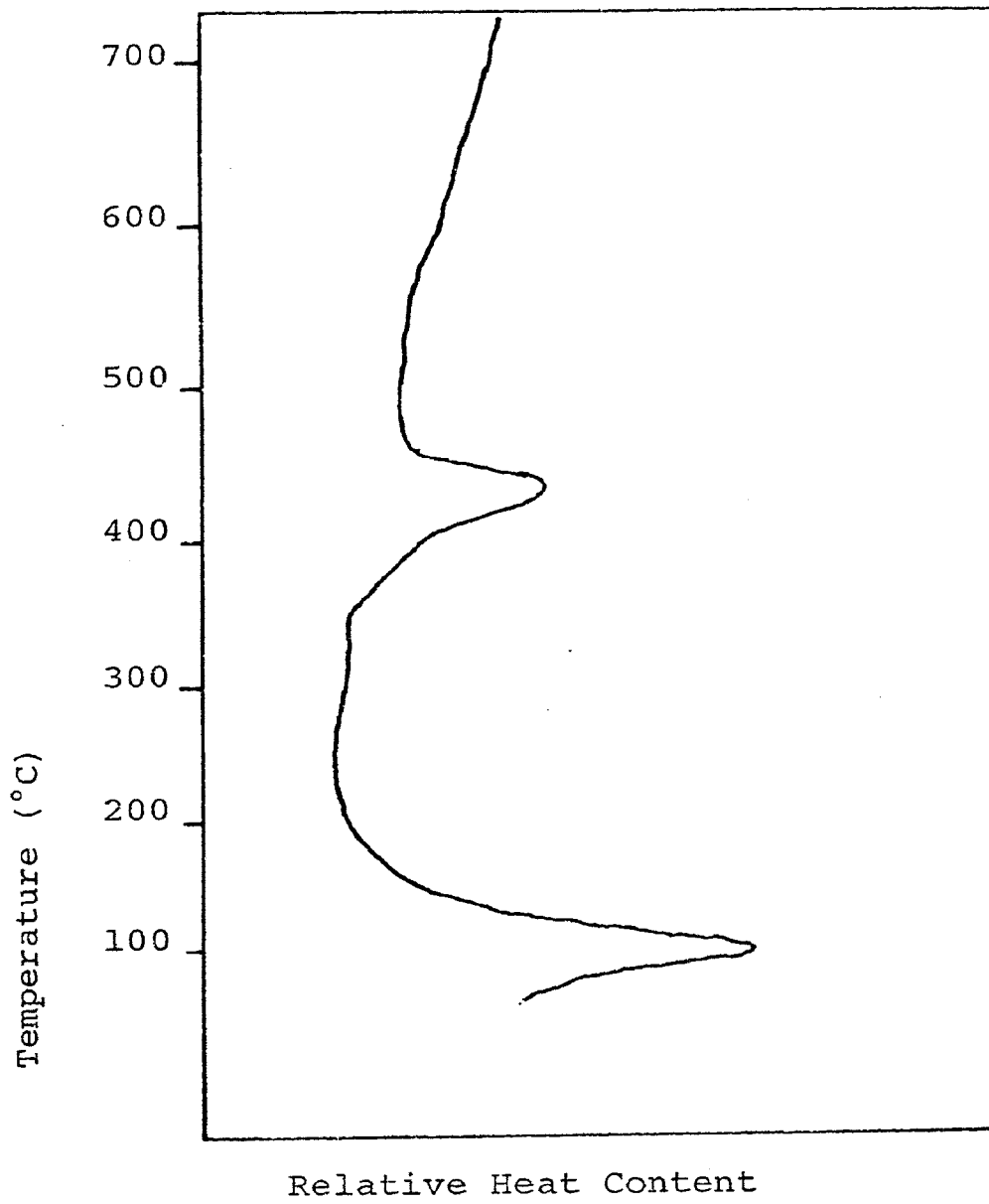
Figure D-3. DTA Curve for Cr(OH)$_3$ Gel
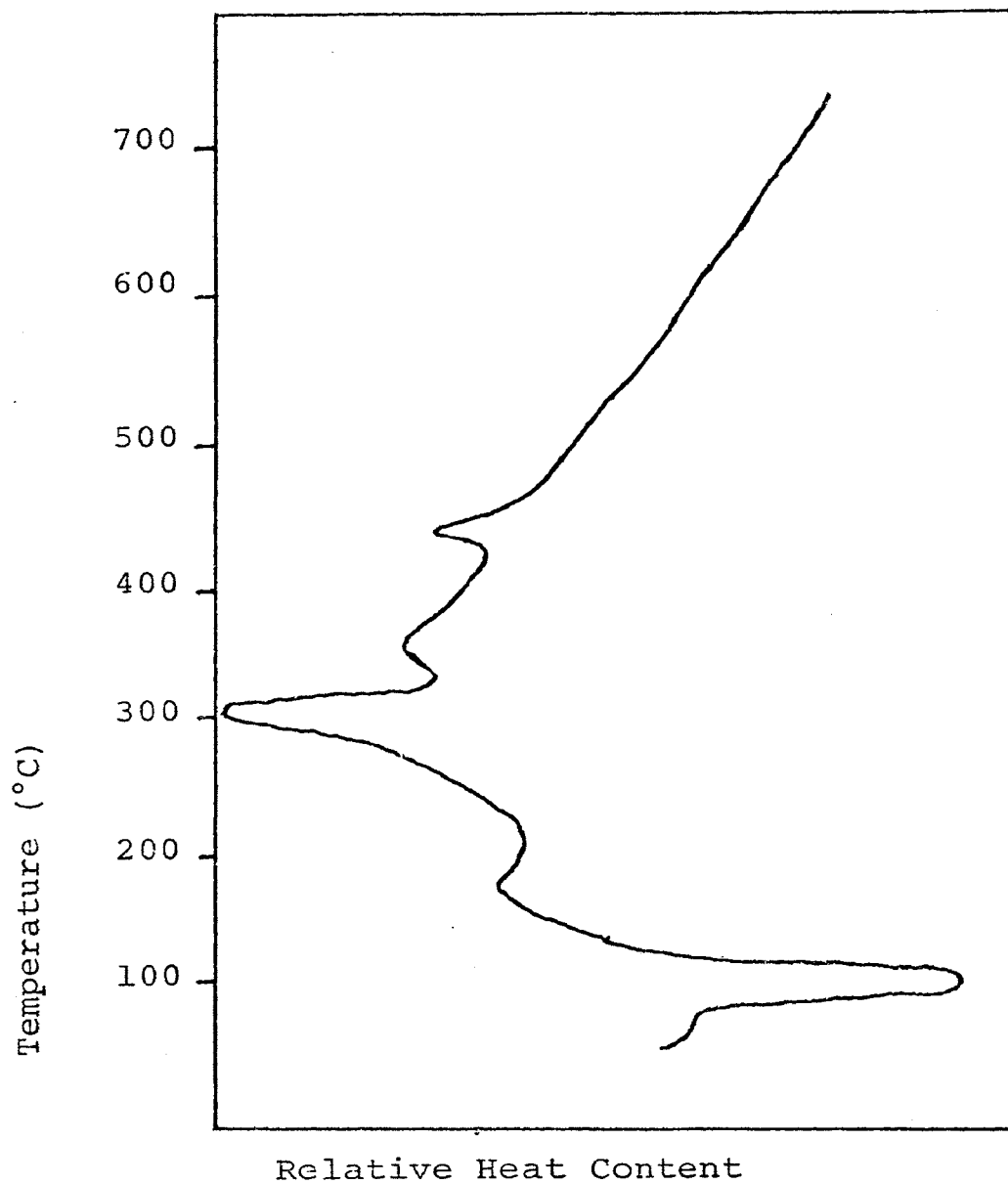
Figure D-4.   DTA Curve for Synthesized
              $Cr(OH)_3$

APPENDIX E.

Table E-1.

Analysis of Variance of Linear Regression
of Arrhenius Plot for Crystallite Growth Rate

Source of Variation	Degree of Freedom	Sum of Squares	Variance	F-Ratio	Significance
Linear Regression	1	.6574	.6574	1095	$\alpha = .001$
Residual	2	.0012	.006		
Total	3	.6586	----		

The regression analysis explains 99.8% of the variance at a 99.8% confidence level.

APPENDIX E.

Table E-2.

Analysis of Variance of Linear Regression
of Arrhenius Plot for Decomposition Rate

Source of Variation	Degree of Freedom	Sum of Squares	Variance	F-Ratio	Significance
Linear Regression	1	.2053	.2053	20	$\alpha = .05$
Residual	2	.0205	.01205	--	
Total	3	.2258	----	--	

The regression analysis explains 90.7% of the variance at a 99.5% confidence level.

APPENDIX F.

Error Analysis

The uncertainty in the furnace temperature was
believed to be the major source of error in the cry-
stallite growth and decomposition studies. Uncertain-
ties in measuring the crystallite diameter and in
measuring the weight of a sample at any given time
were also possible sources of error in determining
the activation energies for crystallite growth rate
and decomposition rate, respectively. The errors in
these activation energies were obtained by differen-
tiating the Arrhenius equation for those two rate
processes.

These expressions were inserted into the probable
error equation:

$$P = \pm \left[\left(\frac{y}{x} \right)^2 (r_x)^2 + \left(\frac{y}{z} \right)^2 (r_z)^2 + \cdots \right]^{1/2}$$

as given by Daniels and Alberty (34). Assuming a temp-
erature uncertainty of five degrees and an uncertainty
of 10 Angstrom units in the crystallite diameter, a
random error of ±1.36 kilocalories per mole results for the
crystallite growth rate. Assuming the same uncertainty
in temperature and an uncertainty of 0.1 milligrams in

sample weight, a random error of ±2.34 kilocalories per mole results for the decomposition process.

BIBLIOGRAPHY

1. S. J. Gregg, "Production of Active Solids by Thermal Decomposition, Part 1. Introduction," J. Chem. Soc. 4, 3940 (1953).

2. C. Hyde and W. Duckworth, "Investigation of Sinterable Oxide Powders," WADD Tech. Rept., Wright-Patterson AFB, Ohio, 61-262, (1961).

3. E. A. Rosauer and R. L. Handy, Iowa Academy of Science 68, 357 (1961).

4. Y. Harada, Y. Bashin and J. H. Handwerk, "Calcination and Sintering Study of Thoria," J. Am. Ceram. Soc. 45 (6), 253-257, (1962).

5. L. R. Furlong and L. P. Dominques, "Sintering of Yttrium Oxide," B. Am. Ceram. Soc. 45 (12) 1051-1054 (1962).

6. R. C. Rau, "Calcination of BeO from Basic Acetate Derived Be(OH)$_2$", J. Am. Ceram. Soc. 47 (4) 179-184 (1964).

7. R. A. Brown, "Sintering in Active Nickel Oxide," J. Am. Ceram. Soc. 48 (12) 627-630 (1965).

8. S. J. Gregg, R. K. Packer and K. H. Wheatley, "Production of Active Solids by Thermal Decomposition. Part IV. Sintering of Active Magnesium Oxide," J. Chem. Soc. 46-50 (1955).

9. P. W. M. Jacobs and F. C. Tompkins, Chemistry of the Solid State. Chpt. 7, Edited by W. E. Gamer (Butterworths, London, 1955).

10. T. Langmuir, "The Constitution and Fundamental Properties of Solids and Liquids, Part 1. Solids, "J. Amer. Chem. Soc., 38 2263 (1916).

11. K. L. Mampel, "Zeitumstayformelin fur heterogene Reaktionen an Phasengrengen fester Korper," Z. Physik. Chem. A187 43 235 (1940).

13. C. Eyraud and R. Goton, J. Chim. Phy. $\underline{51}$, 430-433 (1954).

14. W. D. Callister, I. B. Cutler and R. S. Gordon, "Thermal Decomposition Kinetics of Boehmite," J. Am. Ceram. Soc. $\underline{49}$ (8) 419-422 (1966).

15. R. S. Gordon and W. D. Kingery, "Thermal Decomposition of Brucite: II, Kinetics of Decomposition in Vacuum," J. Am. Ceram. Soc. $\underline{50}$ (1) 8-14 (1967).

16. P. J. Anderson and D. T. Livey, "Physical Methods for Investigating the Properties of Oxide Powders in Relation to Sintering" Powder Metallurgy No. 7, 189-203 (1961).

17. P. Murray, "Active Ceramic Oxide Powders," Agglomeration 93-111, Edited by W. A. Knepper (Interscience Publishers, New York, 1962).

18. K. Iwase, T. Takada and T. Hayashi, "Sintering and Crystallographic Characteristics of Fine Oxide Particles Produced by Calcination," Sintering Symposium, Austral. Inst. of Min. and Met., 1958.

19. G. C. Kuczynski, "Self-Diffusion in Sintering of Metallic Particles," Trans. Am. Inst. Min. Met. Engrs., $\underline{185}$, 169-178 (1949).

20. N. Caberra, "Sintering of Metallic Particles," Trans. Am. Inst. Min. Met. Engrs., $\underline{188}$, 667-668 (1950).

21. C. Herring, "Effect of Change of Scale on Sintering Phenomena," J. Appl. Phys., $\underline{21}$ (4) 301-303 (1950).

22. W. D. Kingery and M. Berg, "Study of Initial Stages of Sintering Solids by Viscous Flow, Evaporation-Condensation and Self-Diffusion," J. Appl. Phys., $\underline{26}$ (10) 1205-1212 (1955).

23. W. C. Hagel and A. V. Seybolt, "Cation Diffusion in Cr_2O_3," J. Electrochem Soc. $\underline{108}$ (12) 1146-1152 (1961).

24. W. C. Hagel, "Anion Diffusion in Cr_2O_3," J. Am. Ceram. Soc., $\underline{48}$ (2) 70-75 (1965).

25. W. C. Hagel, P. J. Jorgenson and D. S. Tomalin, "Initial Sintering of Cr_2O_3," J. Am. Ceram. Soc., 49 (1) 23-26 (1966).

26. A. W. Laubengayer and H. W. McCune, "New Crystalline Phases in the System Chromium Oxide-Water," J. Am. Chem. Soc., 74 (5) 2362-2364 (1952).

27. R. Roy and M. W. Shafer, "Verbindungsbildung und Phasengleichgewicht in den Systems Cr_2O_3-H_2O, Sc_2O_3-H_2O und Tl_2O_3-H_2O", Zeits fur Anorg. und Alleg. Chem. 276, 275-288 (1954).

28. H. P. Klug and L. E. Alexander, X-ray Diffraction Procedures; pp. 491-537 (John Wiley & Sons, 1954).

29. H. C. Fischer, "Calcination of Calcite: II, Size and Growth Rate of Calcium Oxide Crystallites", J. Am. Ceram. Soc. 38 (8) 284-288 (1955).

30. L. S. Birks and H. Friedman, "Particle Size Determination from X-ray Line Broadening" Jour. of App. Phy. (17) 687-692, (1946).

31. W. D. Kingery, Introduction to Ceramics (John Wiley & Sons, New York, N.Y.) 1960, p. 353.

32. S. J. Gregg and R. I. Razouk, "Kinetics of Thermal Decomposition of Magnesium Hydroxide," J. Chem. Soc. 536-544, (1949).

33. J. L. Margrave, V. V. Dadape, L. H. Dreger and K. Wang, "Sublimation of Cr_2O_3 at High Temperatures," J. Am. Ceram. Soc. 43 (10) 509-510 (1960).

34. F. Daniels and R. A. Alberty, Experimental Physical Chemistry (McGraw-Hill Book Co., N.Y.) 1949, pp. 360-361.

VITA

Timothy A. Clancy was born on September 10, 1940 at Meadville, Pennsylvania. He attended public schools there and in Barnwell, South Carolina, graduating from Barnwell High School in June, 1958. In June, 1962 he received the Bachelor of Science degree in Ceramic Engineering from Clemson University. In August, 1963 he received the Master of Science degree in Ceramic Engineering from Clemson. After working for two years with the National Aeronautics and Space Administration in Houston, Texas, he enrolled in the graduate school of the University of Missouri at Rolla to study for the Doctor of Philosophy in Ceramic Engineering.